Analysis results of the April 1996 combined test of the LArgon and TILECAL barrel calorimeter prototypes

M. Cobal[1], S. Cologna[2], D. Costanzo[2], M. David[3], T. Davidek[4], I. Efthymiopoulos[1], J. Khubua[5,a], Y. Kulchitsky[5,6], M.V. Kuzmin[6], B. Lund-Jensen[7], R. Leitner[4] E. Mazzoni[2], M. Mosidze[5,a], S. Němeček[8], M. Nessi[1], D. Pantea[9], P. Sala[10], A. Solodkov[11], B. Stanek[12], I. Vichou[13]

1) *CERN, Geneva, Switzerland*
2) *INFN, Pisa University and Scuola Normale Superiore, Pisa, Italy*
3) *LIP and University of Lisbon, Portugal*
4) *Faculty of Mathematics and Physics, Charles University, Prague, Czech Republic*
5) *JINR, Dubna, Russia*
6) *Institute of Physics, National Academy of Sciences, Minsk, Belarus*
7) *KTH, Stockholm, Sweden*
8) *Institute of Physics of ASCR, Praha, Czech Republic*
9) *NIPNE Bucharest, Romania*
10) *INFN and University of Milan, Italy*
11) *LPC Clermont-Ferrand, Université Blaise Pascal CNRS-IN2P3, France*
12) *Argonne National Laboratory, USA*
13) *Institut de Fisica d'Altes Energies, Universitat Autonoma de Barcelona, Spain*

Abstract

In April 1996 a second combined electromagnetic and hadronic ATLAS calorimeter prototype test beam was performed. The response to pions and electrons of various energies (10, 20, 40, 50, 80, 100, 150 and 300 GeV) at an incident θ angle of 12^0 was investigated. The energy released by pions in the prototype was reconstructed using a minimal set of corrections introduced to take into account various detector effects ("benchmark" approach). A weighting method 'a la H1' was applied too. Energy resolution, e/π and linearity were calculated. Finally, the transverse and longitudinal pion shower developments were examined as well as the longitudinal leakage. The signal released by muons was analyzed. The noise was evaluated for both the detectors. The results were compared with those obtained in the previous combined test beam, performed in September 1994.

---

[a]On leave from High Energy Physics Institute of Tbilisi State University, Georgia.

Contents

1 The ATLAS calorimeter prototypes

The ATLAS detector [1] will include a barrel liquid argon (LAr) electromagnetic (EM) calorimeter, with hermetic accordion geometry, and a scintillating-tile hadronic calorimeter, using iron as absorber material.

1.1 The EM prototype

The electromagnetic LAr calorimeter prototype, described in detail in [2], consists of a stack of two azimuthal modules, each one spanning $9°$ in azimuth and extending over 2 m along the z direction. The calorimeter structure is defined by 2.2 mm thick steel-plated lead absorbers, folded to an accordion shape and separated by 3.8 mm gaps, filled with liquid argon; the signals are collected by Kapton electrodes located in the gaps. The calorimeter extends from an inner radius of 131.5 cm to an outer radius of 182.6 cm, representing (at $\eta = 0$) a total of 25 radiation lengths (X_0), or 1.22 interaction lengths (λ) for protons. The calorimeter is longitudinally segmented into three compartments of 9 X_0, 9 X_0 and 7 X_0, respectively. The $\eta \times \phi$ segmentation is 0.018×0.02 for the first two longitudinal compartments and 0.036×0.02 for the last compartment. Each read-out cell has full projective geometry in η and in ϕ. The calorimeter was located inside a large cylindrical cryostat with 2 m internal diameter, filled with liquid argon. The cryostat is made out of a 8 mm thick inner stainless-steel vessel, isolated by 30 cm of low-density foam (Rohacell), itself protected by a 1.2 mm thick aluminum outer wall. The sketch in figure 1 shows the face of the EM calorimeter as seen by the beam in the first sampling. The beam was not projective during the April 96 run (see next Section).
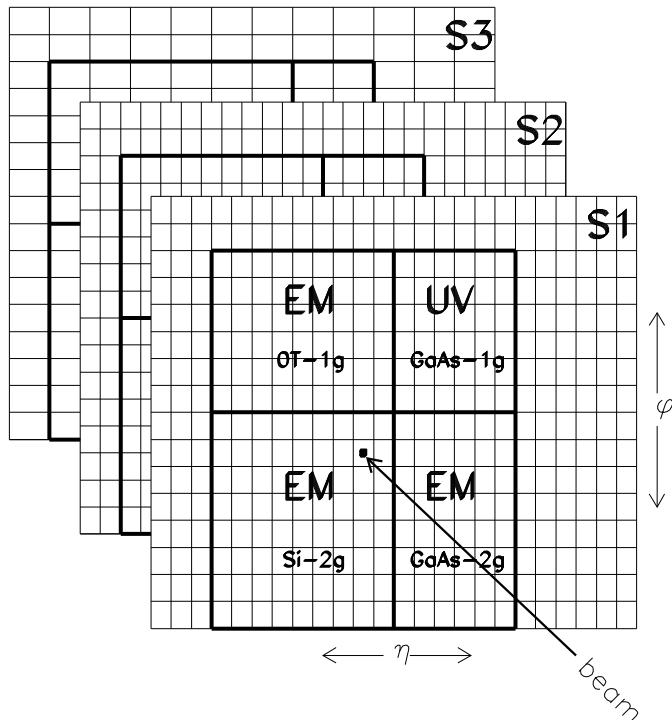

Figure 1: A sketch of the EM calorimeter front face. On each of the three samplings are indicated the regions equipped with a given type of readout electronics. The picture is not projective.

There are four different regions which differs for construction and electronics. The ones called "EM" have the shown granularity for all the samplings except the 3rd one where the cells are double size in η. The part called "UV" has a more shallow first sampling ($\approx 5X_0$'s) which plays the role of the preshower (present in the September 1994 combined run) having very fine granularity in U and V [1]. The whole UV part (sampling 1) has two ϕ parts and for each one of them there are 46 U and 46 V strips. In the LAr (and ntuples) nomenclature samplings 1 and 2 for the UV part are the V and the U-type strips respectively in the actual sampling 1. In the same part, sampling 2 and 3 have the same granularity as the relevant EM part.

Concerning the front-end electronics, the preamplifiers were different for the four regions (Si, GaAs and 0T) and in two of them bigain shapers where used.

The nominal beam impact cell for the first sampling is marked in the sketch with XX. The available reading area is of a maximum of 13 cells in η and 13 cells in ϕ. For the analysis described in this paper only part of the calorimeter was used, namely a matrix of 11×11 cells centred around the nominal beam spot for the first two longitudinal compartments and of 5×11 cells for the third. This corresponds to a front face of about 25×25 cm^2.

Cells in the middle and back samplings of the UV region are added to make up the full 11x11 cell matrix, while the the U and V strips are not used in the reported analysis.

1.2 The presampler

A presampler was mounted in front of the EM calorimeter. The presampler has fine strips in the η direction and covers $\approx 11 \times 8$ in $\eta \times \phi$ EM cells in the region of the beam impact. It has 64 strips in η and 2 cells in ϕ.

The active depth of liquid argon in the presampler was 10 mm and the strip spacing 3.9 mm. The mounting of the presampler was such that the low η part of the beam spot corresponding to $\eta_{cell} < 22.8$ in EM sampling 1 missed the presampler. Cuts were applied to remove such events.

1.3 The hadronic prototype

The hadron calorimeter (Tilecal) prototype consists of an azimuthal stack of five modules. Each module covers $2\pi/64$ in azimuth and extends 1 m along the z direction, such that the front face covers 100×20 cm^2. The radial depth, from an inner radius of 200 cm to an outer radius of 380 cm, accounts for 8.9 λ at $\eta = 0$ (80.5 X_0). Read-out cells are defined by grouping together a bundle of fibres into one photomultiplier (PMT). Each of the 100 cells is read out by two PMTs and is fully projective in azimuth (with $\Delta\phi = 2\pi/64 \approx 0.1$), while the segmentation along the z axis is made by grouping fibres into read-out cells spanning $\Delta z = 20$ cm ($\Delta\eta \approx 0.1$) and is therefore not projective. Each module is read out in four longitudinal segments (corresponding to about 1.5, 2, 2.5 and 3 λ at $\eta = 0$). More details of this prototype can be found in Refs. [1],[3],[5],[6]. With respect to the September 1994 combined test beam, a new element is present. In order to try to understand the energy loss in dead material between the active part of the LAr and the Tilecal detectors a layer of scintillator was installed, called the midsampler. The midsampler consisted of five scintillators, 20 cm $\times$ 100 cm each, fastened directly to the front face of the Tilecal modules. The scintillator was 1 cm thick, and was readout using ten 1 mm WLS fibers on each of the long sides. The beam incident angle was, as in the previous combined run, near 11^0, but now the impact point was 8 cm left from the center to avoid side leakage.

2 Experimental setup and test beam data

To simulate the ATLAS setup, the Tilecal calorimeter was placed on a fixed table, just behind the LAr cryostat, as shown in figure 2.

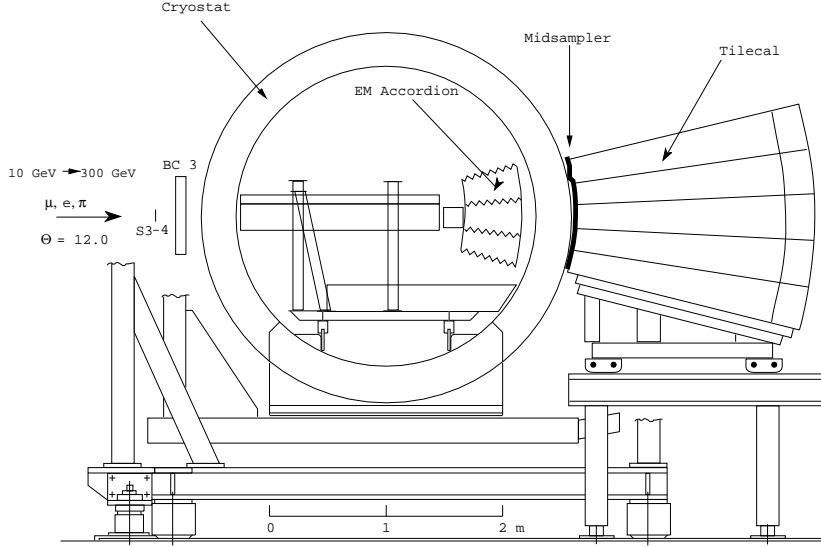[1] U and V are linear combination of η and ϕ.

Figure 2: Test beam setup for the combined LAr and Tilecal calorimeter combined run.

Originally, the impact point was designed to be in $\eta_{cell} = 25$, $\phi_{cell} = 8$ in the first sampling of the EM calorimeter, with an incident angle of about 11^0. Due to an error in the installation, it was discovered that there was an horizontal shift of the EM detector inside the cryostat. Using the bending magnets upstream of the setup, it was possible to recover the required conditions, by directing the beam to the middle of cell 23 in η and 6.7-7 in ϕ, with a small change in the incident angle towards the value of 12^0. This point is in the region equipped with Si double-gain type pre-amplifiers.

By moving the EM calorimeter to the rear of the cryostat, the setup was no longer projective in η and the beam impact point shifted by about 0.015 η units (almost ~cell size in sampling 1 and 2) per sampling. Since this prevented true towers to be used in the analysis, the centre cell for a cluster in each sampling was selected by extrapolating the beam trajectory as measured by beam chambers.

Early showers in the liquid argon were kept to a minimum by placing light foam material in the cryostat upstream of the calorimeter. Beam quality and geometry were monitored with a set of beam chambers and trigger hodoscopes placed upstream of the LAr cryostat. The momentum bite of the beam was always less than 0.5%. Single-track pion events were selected offline by requiring the pulse height of the beam scintillation counters and the energy released in the presampler of the electromagnetic calorimeter to be compatible with that of a single particle. Beam halo events were removed with appropriate cuts on the horizontal and vertical positions of the incoming track impact point as measured with the two beam chambers.

For this layout the effective distance between the two active parts of the detector is of the order of 50 cm, instead of the 25 cm as foreseen in the ATLAS setup. The amount of material in between the two calorimeters has been quantified to be about $2X_o$. This value is similar to the ATLAS design value, but the material type is different: steel instead of aluminum for the cryostat.

The total depth corresponds to about 10.1 λ, to be compared with the 9.6 foreseen in the ATLAS setup [1]. The effective calorimeter depth for pions travelling at a θ angle of 12° is of 10.3 λ.

A large scintillator wall ("muon wall") [7] covering about 1 m^2 of surface has been placed on the back of the calorimeter to quantify leakage.

3 Analysis of pion beams

3.1 Data selection

Pion events of different energies (20, 50, 100, 150, 300 GeV) are used in this analysis. On the average about 10^5 events are available for each energy value. The runs have been taken as close as possible in time to avoid changes in the setup or time variations. Analysis cuts are applied in order to reduce the number of events which had an interaction in the material before the electromagnetic calorimeter. To this purpose the beam elements installed in front of the cryostat (3 beam x-y chambers) and the information from the LAr presampler are used. The cuts applied depend in value from the beam energy. Here we report the selection applied in the case of the 300 GeV runs:

- The trigger bit for physics events is required:

  ```
  rndm=0.AND.trig=1
  ```

- Tracks with large angles with respect to the beam direction are removed (units are in mm):

  ```
  bc1_x.gt.0.007.AND.bc1_x.lt.0.015
  bc1_y.gt.-0.019.AND.bc1_y.lt.-0.014
  bc2_x.gt.0.002.AND.bc2_x.lt.0.011
  bc2_y.gt.-0.018.AND.bc2_y.lt.-0.010
  bc3_x.gt.-0.001.AND.bc3_x.lt.0.008
  bc3_y.gt.-0.017.AND.bc3_y.lt.-0.008
  (bc1_x-bc3_x).gt.0.0035.AND.(bc1_x-bc3_x).lt.0.012
  (bc1_y-bc3_y).gt.-0.008.AND.(bc1_y-bc3_y).lt.0.002
  ```

- The signal in the beam scintillator should be compatible with that of a m.i.p.:

  ```
  sc1.gt.250.AND.sc1.lt.600
  sc2.gt.250.AND.sc2.lt.400
  ```

- The energy in the presampler window and cluster are required to be compatible with a m.i.p.:

  ```
  E_pscls.gt.0.0002.AND.E_pscls.lt.0.0045
  E_pswin.gt.-0.015.AND.E_pswin.lt.0.04
  ```

- The impact position (in η units), reconstructed using the presampler detector, is required to match the one evaluated by using the beam chambers information. The distribution of the difference between the two positions has a gaussian core (due to the intrinsic resolution) and tails on both sides. When a pion interacts before entering the presampler, the impact position reconstructed is either due to some particles from the pion shower, or to the presence of the noise. In both cases this impact position is not correlated with the beam chambers impact position. In this way the tails before mentioned can be explained and one can benefit in rejecting the events outside of the distribution core. As a cross check we observe that for events in the tails a smaller energy (using the benchmark method) is reconstructed, if compared with the other events.

  ```
  abs(t_pscls1-t_bepss1+3.533).le.0.9
  ```

3.2 Events which start to shower in the Hadronic calorimeter

In order to check that the Tilecal Calorimeter was performing well during the combined test beam, we studied the energy resolution and linearity obtained for those events which start to shower only in the hadronic calorimeter.

To select these events we required m.i.p. in each sampling of the EM and in the midsampler (the layer of scintillators in front of the hadronic calorimeter). In figure 3 it is shown the m.i.p. requirement for each of the samplings of the EM calorimeter and for the midsampler in the case of 300 GeV pions. The peaks in the energy distribution have been fitted with a Landau and a
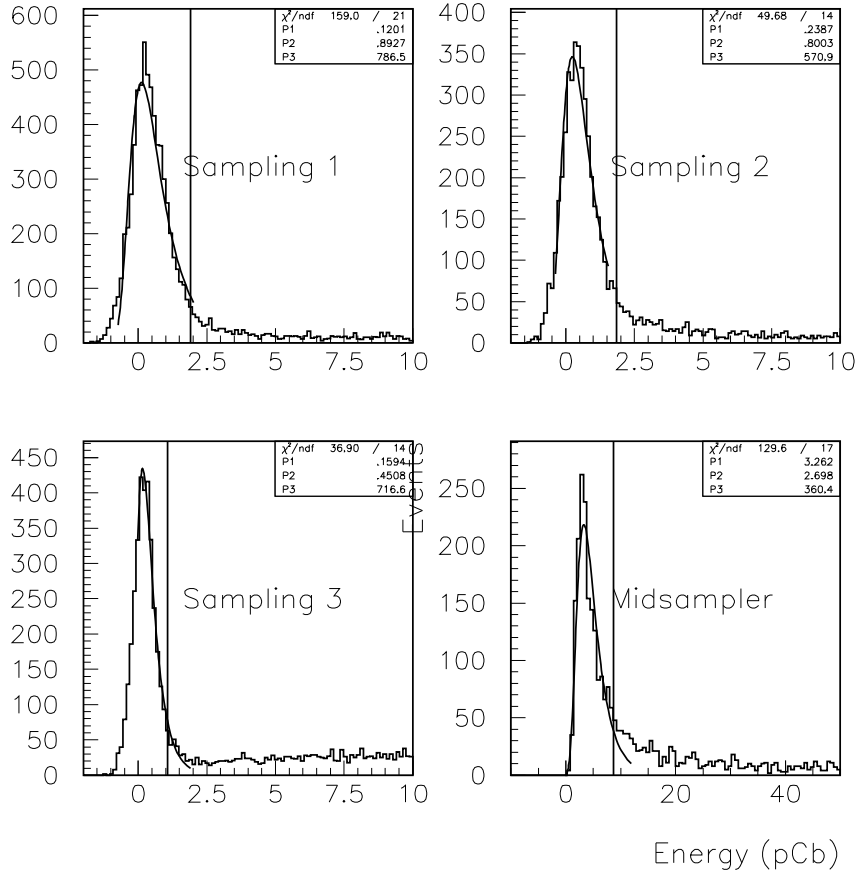
Figure 3: M.i.p. requirement for each sampling of the EM calorimeter and for the midsampler, in the case of 300 GeV pions.

cut was applied at one σ. In figure 4 we report the linearity and resolution obtained for all the energies studied. In the upper plot (linearity) the points are normalized to the 100 GeV case. One can see that the linearity is in agreement with the 1993 Tilecal standalone test beam data results [3], where a run at 12^0 has been investigated. Also for what concern the resolution, the data from the 1996 combined test beam with m.i.p. requirement and 1993 Tilecal standalone test beam are in good agreement.

3.3 Pion energy reconstruction

In the case of the combined test beam data, two particular effects contribute to degrade the energy resolution:

1. The presence of the cryostat between the electromagnetic and hadronic calorimeters. The cryostat is made by passive material in which a certain amount of energy is lost.

2. The non-compensating nature of both the electromagnetic and hadronic calorimeters, which makes the e/π ratio different from 1.

To reconstruct the hadron energy two algorithms were employed. The first method referred to in the following as the "benchmark approach" is designed to be simple [8]. With this method the incident energy is reconstructed with a minimal number of energy-independent parameters. The second method is inspired by the weighting technique [9] used by the H1 experiment.
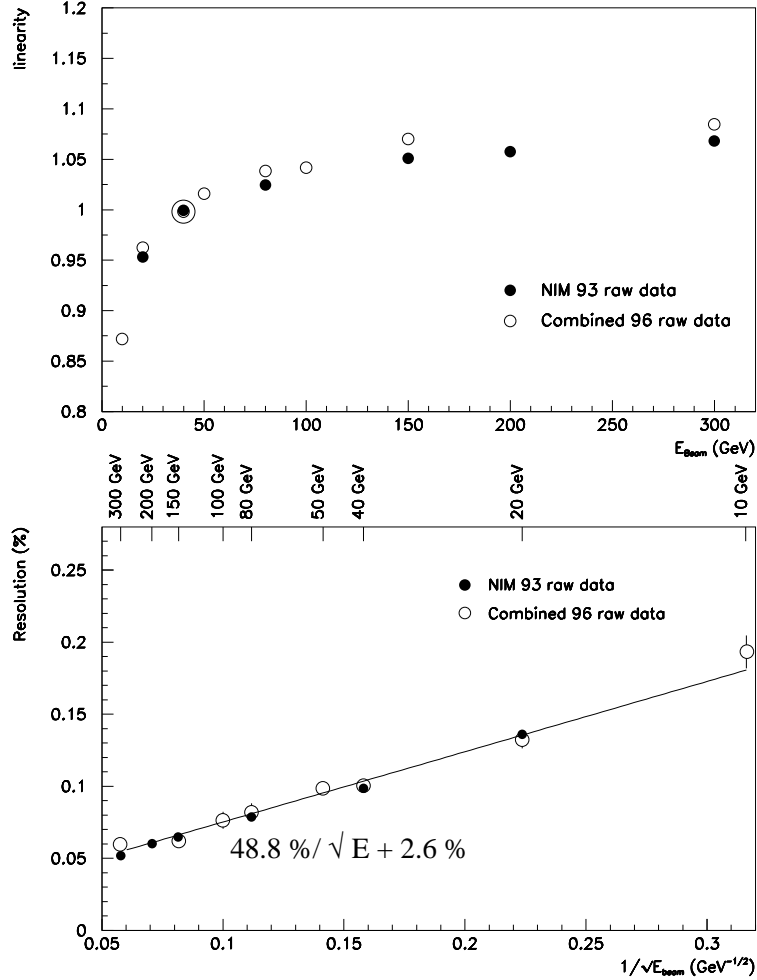
Figure 4: Upper plot: linearity for the 93 Tilecal standalone test beam raw data and for the 1996 combined test beam data requiring m.i.p. in the EM compartment. Lower plot: same comparison for the resolution.

3.3.1 Energy reconstruction using a simple approach as a benchmark.

The benchmark method introduces a set of three energy-independent corrections: the intercalibration between the EM and the hadronic calorimeters, a correction for the energy lost in the cryostat wall separating the two calorimeters, a quadratic correction for the EM calorimeter to

crudely correct its non-compensating behavior and to provide a response independent from the energy released in this compartment. The total reconstructed energy is expressed as:

$$E_{tot} = a \cdot E_{had} + E_{em} + b \cdot E_{em}^2 + c \cdot \sqrt{a \cdot E_{had1} \cdot E_{em3}} \qquad (1)$$

The parameters which weight these corrections are determined by minimizing the fractional energy resolution of 300 GeV pions, and turn out to be equal to: $a = 0.118$, $b = -0.00058$, $c = 0.54$. It has to be recalled that the a parameter in the formula (1) is not a Tilecal calibration constant, but has been found by minimizing the resolution. The parameters are energy independent, The validity of the cryostat correction, expressed as the geometric energy mean of the last LAr sampling energy and the first Tilecal calorimeter sampling energy, has been tested with the midsampler inserted between the cryostat and the Tilecal calorimeter to sample the shower in this region as shown in figure 5.
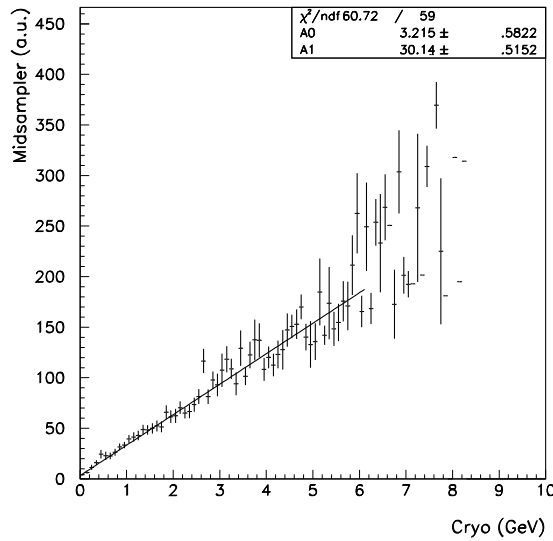

Figure 5: Correlation between the energy released in the midsampler and the cryostat energy as it is defined in the benchmark expression. A good linear correlation is seen in this plot.

In the expression (1), no coefficient is multiplying the LAr energy. Thus we are using as overall normalization the electron LAr energy scale which is downshifted by 92.5 % as will be shown in Section 3.5.

In this analysis we used the energy released in an 11x11 window around the impact position for the LAr calorimeter to compare our results to what has been obtained in 1994. The reconstructed energy distributions for 10, 20, 80 and 300 GeV pions are shown in figure 6. Peak and σ values are extracted with a Gaussian fit over a $\pm 2\sigma$ range. The peak at low energies (3-4 GeV) in the 20 GeV distribution is due to the muon contamination of the pion beam and is present, but out of scale, also for the other beam energies. For the 10 GeV distribution the peak is not visible, since it is hidden in the pions energy tail.

Table 1 summarizes the mean, σ, and energy resolution for the various beam energies.

The combined setup was simulated with the standalone FLUKA [10] program. Details of the simulations have already been reported in [4]. The 10 GeV point has been added with an estimated proton contamination of 14%. The new presampler configuration has been implemented.

In the present work, a deeper care has been taken in the presampler event reconstruction, trying to implement a clustering algorithm as similar as possible to the experimental one. The effectiveness of the presampler veto has also been investigated by varying the cluster size and the noise value. The experimental presampler cluster is made up of three cells along η and 1 in
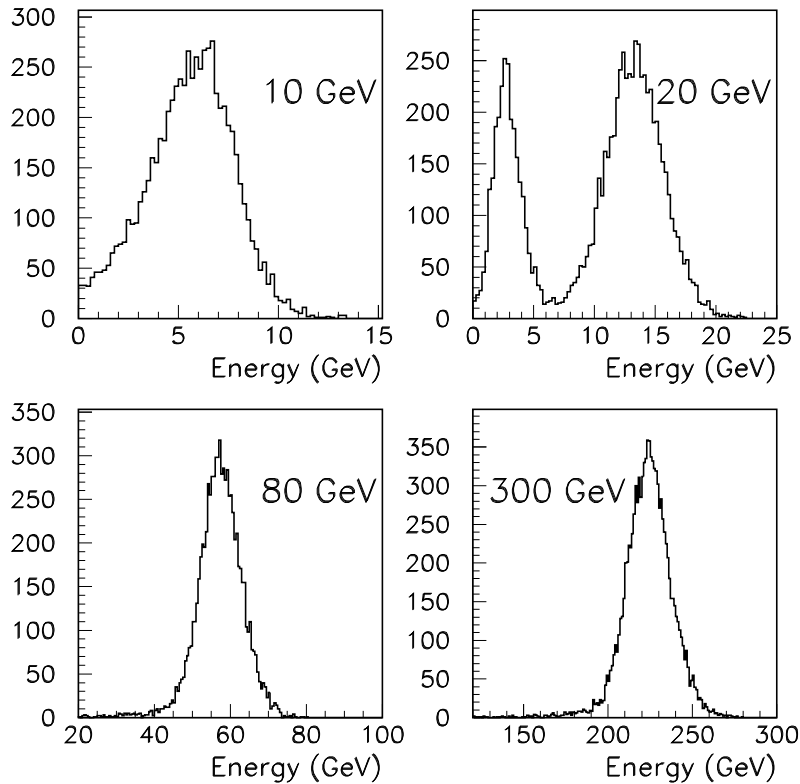
9

Figure 6: Pion energy spectra at different incident energies (benchmark reconstruction).

ϕ, and the cluster center is found by looking for the cell with largest energy in a window around the nominal impact position as defined by the beam chambers. in FLUKA, after the cell-by-cell convolution with the presampler noise. The energy calibration has been made on the minimum ionizing peak. The veto capabilities have been compared with the "ideal" (but unrealistic) situation, that is a noiseless full-width presampler, and with the non-vetoed situation. The fractional energy resolution at 10 GeV (the most affected point) goes from 27.5 % without veto, to 25.3% with the standard veto, and to 24.5% with the "ideal" veto.

Simulated data have been reconstructed with the benchmark technique, with energy independent parameters fixed by minimizing the fractional energy resolution at 300 GeV. Two sets of parameters have been found that give the same fractional energy resolution, and differ mainly in the hadronic energy weight. We will refer to these two sets as $A : a = 0.96, b = 0.33, c = 0.00038$ and $B : a = 0.85, b = 0.3, c = 0.0008$.

The two sets give fractional energy resolutions that are undistinguishable at all beam energies, and reproduce quite well the experimental benchmark values except for the point at 10 GeV (figure 7), where, however, the result is strongly dependent on the effective capability to remove events with interactions in the dead materials upstream and to deconvolve the real pion contribution from the muon contamination. A fit to data points gives a fractional resolution of $[(59.5 \pm 2.6)\%/\sqrt{E} + (1.8 \pm 0.2)] \oplus (2.0 \pm 0.1)/E$ The sampling term is larger with respect to what obtained with 1994 data: $[(52.1 \pm 5.5)\%/\sqrt{E} + (1.9 \pm 0.3)] \oplus (3.2 \pm 0.4)/E$ [4]. However, one should be aware that there is a correlation between the noise term and the sampling one. Decreasing the noise term (thanks to the 20 GeV point) results in an increase of the sampling term.

Energy (GeV)	μ (GeV)	σ (GeV)	$\frac{\sigma}{\mu}(\%)$
10	5.96 ± 0.05	1.79 ± 0.04	30.03 ± 0.72
20	13.30 ± 0.04	2.33 ± 0.04	17.52 ± 0.30
40	27.91 ± 0.07	3.42 ± 0.08	12.25 ± 0.29
50	35.42 ± 0.06	3.91 ± 0.06	11.04 ± 0.17
80	57.44 ± 0.08	5.03 ± 0.09	8.75 ± 0.16
100	72.13 ± 0.10	5.94 ± 0.09	8.23 ± 0.13
150	111.24 ± 0.12	7.44 ± 0.14	6.69 ± 0.13
300	223.54 ± 0.16	11.66 ± 0.20	5.21 ± 0.09

Table 1: Mean energy, σ and energy resolution for the various beam energy, using the benchmark approach.
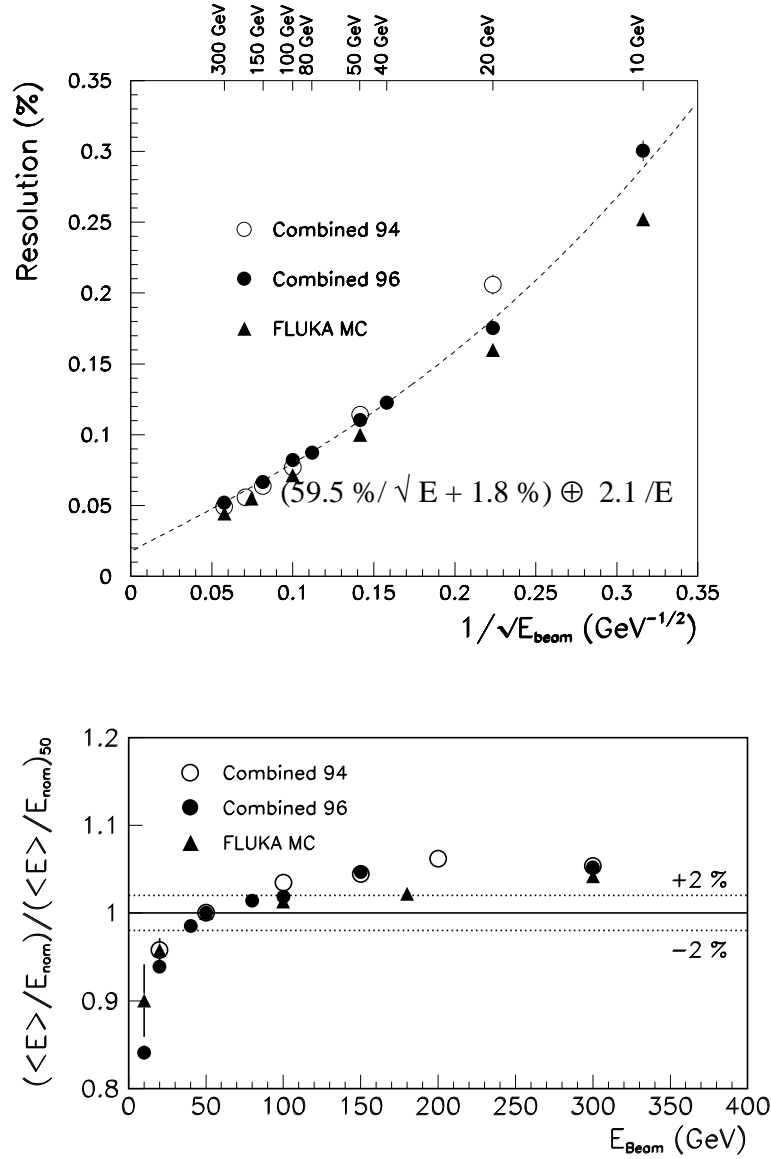

Figure 7: Upper plot: fractional energy resolution. Lower plot: relative non-linearity as a function of beam energy. Points are normalized to the 50 GeV one.

3.3.2 Energy reconstruction using the 'H1 method'

The H1-inspired weighting technique is based on correcting upwards the response of cells with relatively small signals, to equalize their response to that of cells with large (typically electromagnetic) deposited energies. All the instrumented window of the LAr calorimeter have been used for this analysis. This method has succesfully applied to the combined 1994 data as described in reference [9]. There an exhaustive description of the method can be found while here we will describe only its main features.

The total energy is reconstructed correcting the energy in each cell of either calorimeter by a factor (typically > 1) which is a function of the energy in each cell and of the beam energy. A correction for the energy loss in the cryostat is also applied. Thus the total energy can be expressed as:

$$E = \sum_{em.cells} W_{em}(E_{cell}, E_{beam}) \cdot E_{cell} + \sum_{had.cells} W_{had}(E_{cell}, E_{beam}) \cdot E_{cell} + \text{cryo} \qquad (2)$$

In this expression the energy contributions from LAr cells are expressed in GeV while those from Tilecal cells are in pCb. The cryostat term is the same as the one used for the benchmarks technique described in the previous section.

As a first step we evaluate the optimal weights (in terms of resolution and linearity) for each beam energy without taking into account that this information is not available in real life. To explain how such weights are evaluated we discuss what has been done for the 150 GeV π^+ case, the same will apply for all the other beam energies.

At a fixed beam energy we have to give a parametrization of the weights W_{em} and W_{had} by the cell energy but, at first sight, it's not so easy to guess a function which could give a good parametrization. To solve this problem we divide the cells' energy spectra in equally populated intervals and, for each of such intervals, a weight W_i is assigned. Thus, by minimizing the energy resolution, we choose for each W_i a numerical value. Finally the weights are plotted against the mean energy released in the correspondent $i - th$ interval as shown in figure 8.

At this point we can express W_{em} and W_{had} in the following way:

$$W_{em} = A_E + B_E/E_{cell} \qquad (3)$$
$$W_{had} = A_H + B_H/E_{cell} \qquad (4)$$

Where A_E, B_E, A_H and B_H are taken from a fit to the points in figure 8.

The same exercise has been repeated for all the available beam energies: the same interval definition was always used to avoid biases. As a result we are left with a set of 4 parameters (A_E, B_E, A_H and B_H) for each beam energy (i.e. $4 \times 8 = 32$ parameters).

Having exploited the weights dependence on the cell energy, we studied the dependence on the beam energy. To do this we further parametrize the A_E, B_E, A_H and B_H as a function of beam energy as shown in figure 9. The total number of parameters is reduced to 8 (adding the cryostat constant).

The values for A_h and B_h obtained for the 10 GeV point are not used in the parametrization since, at this energy, it is not easy to discriminate muons from pions. This is seen in Tilecal since most of the pions cannot deeply penetrate the calorimeter, while muons release energy also in the last hadronic samplings. Anyway we will show how the extrapolation of the weighting parameters to 10 GeV gives good results.

With the chosen 8 parameters (including the cryostat constant) we obtain a good fractional resolution and linearity, but we are still using the beam energy knowledge.

The problem of the dependence on the beam energy is solved in this way:

1. Define the reconstructed energy as $1.35 \cdot E_{bench}$ and use it to evaluate weights, instead of the 'true' beam energy. We choose 1.35 as the factor needed to have a mean response of 300 GeV for 300 GeV pions.
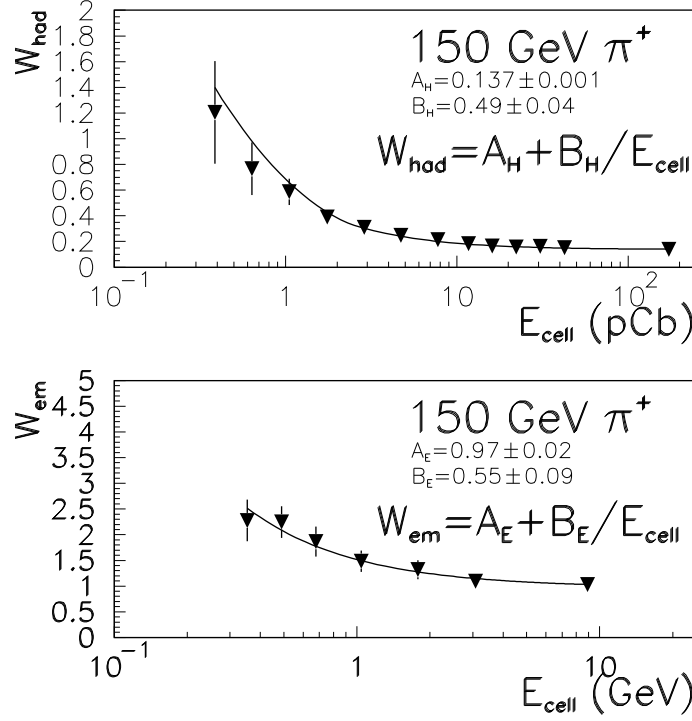
Figure 8: Weight values for different energy intervals (150 Gev pions). The upper plot refers to the Tilecal calorimeter, the bottom one to LAr. The chosen parametrization is also shown.

2. Run the H1 weighting algorithm

3. Recompute the weights using the energy reconstructed in point 2.

4. Iterate this procedure until stable results are obtained.

It turns out that after three iterations the reconstructed energy is stable within few tens of MeV.

The fractional resolution as well as the linearity obtained after this procedure are reported in figure 10. The resolution is fitted by the function:

$$[\frac{(41.9 \pm 1.6)\%}{\sqrt{E}} + (1.8 \pm 0.1)\%] \oplus \frac{1.8 \pm 0.1}{E} \tag{5}$$

which is in good agreement with the result obtained for the 1994 data [9]:

$$[\frac{(38.3)\%}{\sqrt{E}} + (1.62)\%] \oplus \frac{3.06}{E} \tag{6}$$

The noise term is lower and the sampling term is a little bit higher as already noticed with the benchmark method.

3.3.3 High energy tails

In the two previous sections we studied the quality of pion energy reconstruction by fitting (in a limited interval of about 2σ) the distributions of the reconstructed energy with a gaussian function. It is also worth understanding the behaviour of such distributions far away from their core where we experience some deviations from the gaussian shape (tails). Events belonging to a tail can be dangerous since they can contribute to a wrong evaluation of jet or missing energy, causing an instrumental background to many physics signatures.
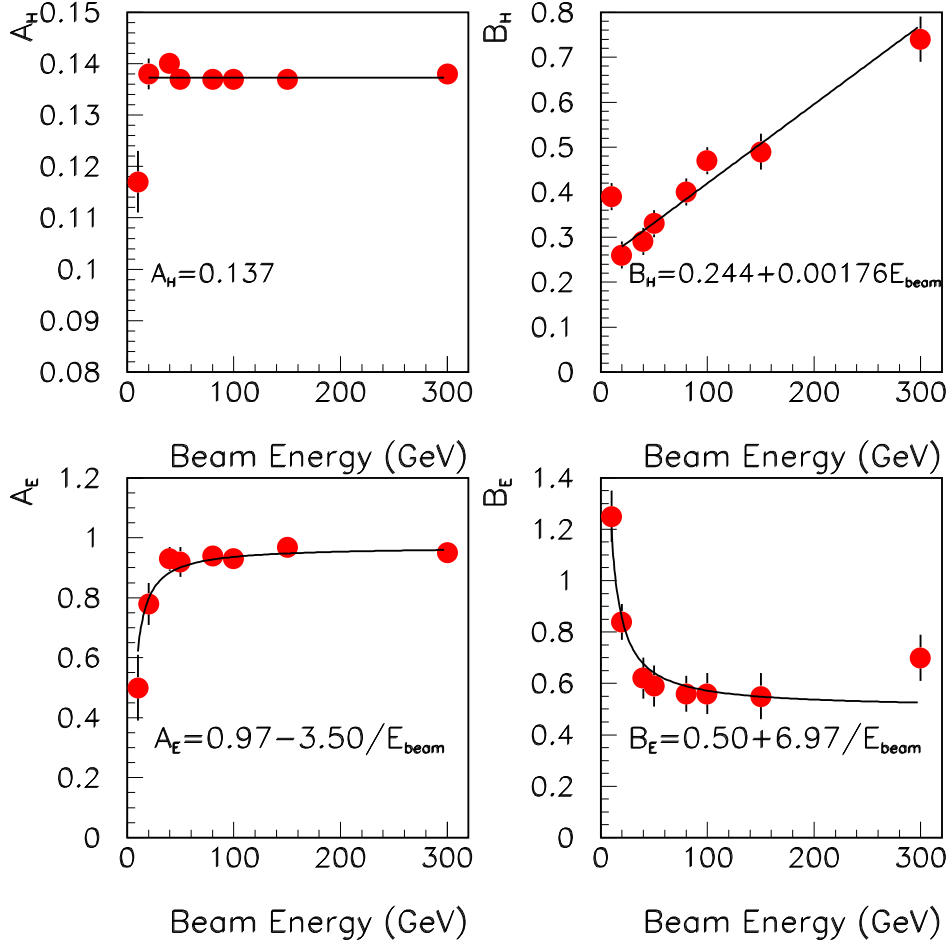
13

Figure 9: Beam energy dependence for the parameters A_E, B_E, A_H and B_H. In each figure the used parametrization is shown.

We divide the study of these tails into two parts: high energy tails (due to the intrinsic non-gaussian characteristic of hadronic showers) and low energy tails (due to punchthrough particles in the shower).

In order to quantify the events which are in the high tails of the reconstructed energy distribution, the percentage of events at more than a certain number of σ from the mean value of the distribution itself has been calculated. The numbers are reported in Table 2 for 300 GeV pions and in Table 3 for 20 GeV pions using the benchmark algorithm. The normalization is done with respect to the number of events under the gaussian fit (in order not to take into account the muon contamination and the energy leakage in the low energy region of the spectra). The tail percentages are shown for an "ideal gaussian" with mean and σ equal to the gaussian which fit the data , for the data itself and for the Fluka Monte Carlo simulated events. One can notice that, inside the statistics, data and Monte Carlo are in reasonable agreement, both showing the presence of high energy tails. The events with energy greater than 3.5 σ in addition to the mean, have been studied one by one. Figure 11 shows a display of Event 4787/Run 11652 (a 300 GeV pion) , which has a reconstructed energy of 279 GeV, more than 4 σ away from the mean value ($\mu = 223.5\,\mathrm{GeV}$ and $\sigma = 11.7\,\mathrm{GeV}$). This event looks like an electromagnetic one indicating that we have a big fraction of em energy released during the shower development as can be noticed by comparing its shower profile with that of a typical event which is a m.i.p. in the
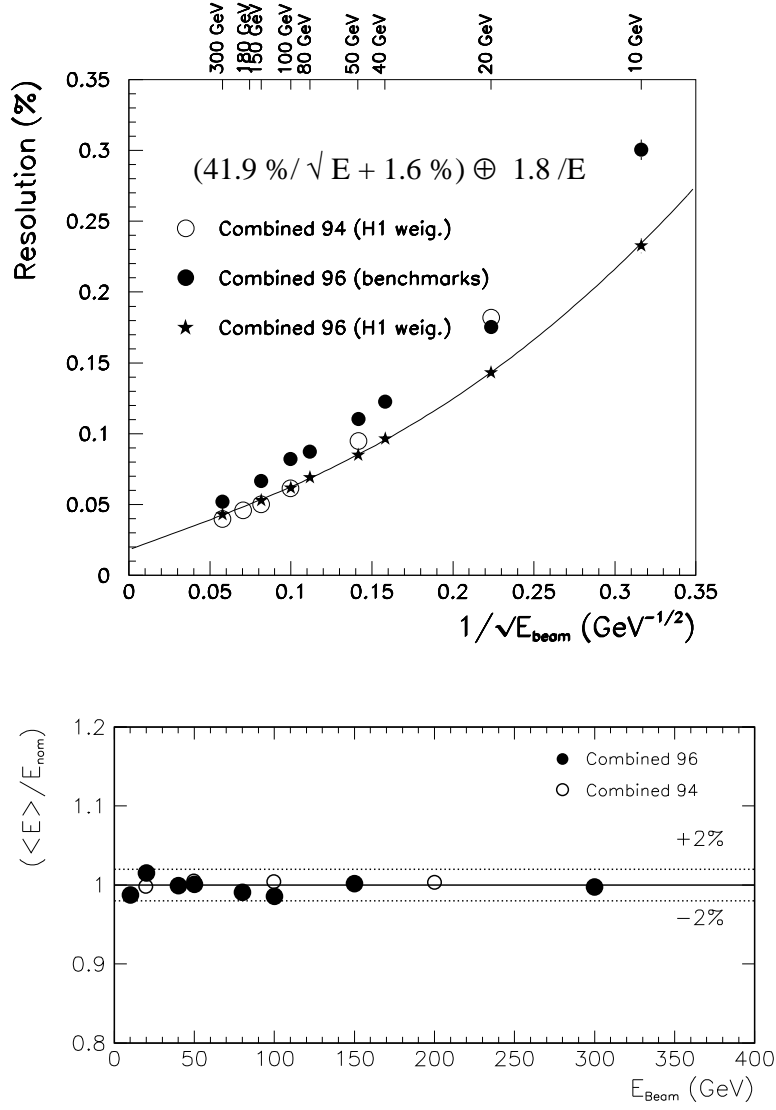
14

Figure 10: Upper plot: fractional energy resolution comparing with 1994 and benchmark results. Lower plot: linearity as a function of beam energy. The H1 weighting technique was used.

electromagnetic calorimeter (shown in figure 12). All the other events look similar to this one, with the exception of another very interesting event in the tails: Event 13168/Run 11685. This event releases an energy of 402 GeV in the calorimeter. The energy is mostly deposited in the hadronic compartment (393 GeV), while only about 4 GeV can be found in the electromagnetic part (there is only one presampler cell with energy above noise and only one EM calorimeter cell with E>150 MeV, namely 300 MeV).

For this event it was checked that it is a single-particle, by looking at the presampler and beam chambers info, and that both the left and right PMTs of the two high energy cells give a similar signal. At the moment we do not understand how such a high energy release was possible.

Figure 14 shows the energy spectra for 300 GeV pions reconstructed with the benchmark technique (plot above) as well as with the H1 technique (plot below). The gaussian means are re-normalized to 300 GeV. The 13 events with energy greater than 360 GeV are shown in grey color. The overflow is the above mentioned Event 13168/Run 11685.

The event is shown in Figure 13.

	Data evts	Expected %	Data %	MC %
all	10247			
> 1.0 σ	1627	15.9	15.9	16.4
> 1.5 σ	786	6.7	7.7	7.0
> 2.0 σ	329	2.3	3.2	2.9
> 2.5 σ	114	0.62	1.1	0.84
> 3.0 σ	47	0.13	0.46	0.41
> 3.5 σ	18	0.023	0.18	0.06
> 4.0 σ	4	0.0032	0.039	-
> 4.5 σ	1	0.0003	0.010	-
> 5.0 σ	1	0.0003	0.010	-

Table 2: Percentage of events at several standard deviations from the mean value of the reconstructed energy distribution using the benchmark algorithm, for pions at 300 GeV.

	Data evt	Expected %	Data %	MC %
all	5943			
> 1.0 σ	950	15.9	16.0	16.5
> 1.5 σ	430	6.7	7.2	6.9
> 2.0 σ	158	2.3	2.7	2.2
> 2.5 σ	55	0.62	0.92	0.62
> 3.0 σ	18	0.13	0.30	0.16
> 3.5 σ	6	0.023	0.10	0.06
> 4.0 σ	0	0.0032	0	0.02
> 4.5 σ	0	0.0003	0	0.01
> 5.0 σ	0	0.00003	0	-

Table 3: Percentage of events at several standard deviations from the mean value of the reconstructed energy distribution using the benchmark algorithm, for pions at 20 GeV.

3.4   Shower leakage studies

In this section we study the tails arising on the low energy side of the reconstructed energy distributions. The presence of those tails indicate that the total energy of a pion can be under extimated since some particles of the shower leak out of the calorimeters. Those punchthrough particles can be muons from π and K decays in a hadronic cascade, or charged particles (mainly soft electrons and hadrons) and neutrons from showers not fully contained in the calorimeter. For this study, pions in the range 40-300 GeV were examined.

The probability of longitudinal shower leakage (P_{punch}) was defined as the fraction of events with a signal in at least one of the muon wall counters. To be considered as a punchthrough signal, the signal Q_i in any counter must satisfy the requirement

$$Q_i > (\overline{Q}_i^{\mu} - 3\sigma_i^{\mu}). \tag{7}$$

The average ($\overline{Q}_i^{\mu}$) and sigma values (σ_i^{μ}) were determined using the most probable energy deposition of muons in the muon wall. Since the μ wall does not cover the whole back of the calorimeter, an evaluation of the acceptance of the μ wall was performed. In table 4 we report the punchthrough probability (P_{punch}) already corrected for the acceptance in 1994 and 1996 data (the acceptance is also shown in the table). It can be seen that the acceptance in 1996 is inceased with respect to 1994, due to a better coverage of the calorimeter.

Figure 15(a) shows the probability of longitudinal shower leakage as a function of the beam energy. The probability is corrected for the acceptance which is around 51% -53%. At 100

GeV this probability is about 11%. The result is compared with what obtained in 1994. The measurements are in agreement (inside errors), but the 1996 data are systematically below, i.e., a slightly lower punchthrough probability is observed over all the energy range.

Figure 11: Display of an event which has a benchmark reconstructed energy of 279 GeV, more than 4 σ away from the mean value. The top lego plots show the energy released in the three EM compartments, while the bottom one has the energy released in the four hadronic sections.

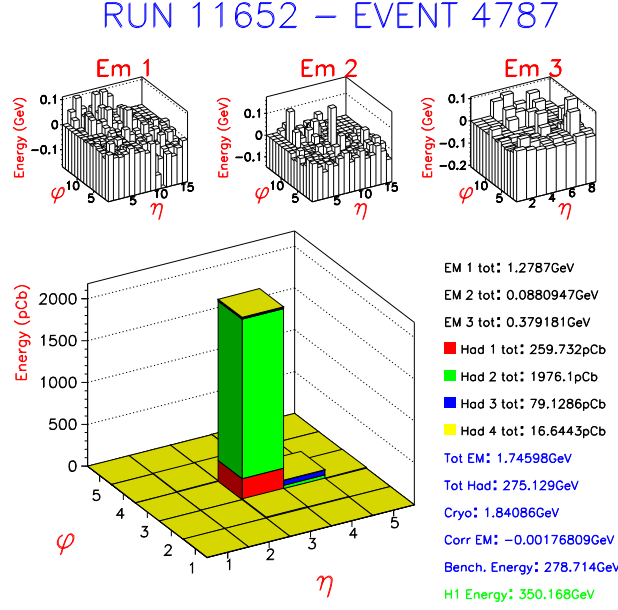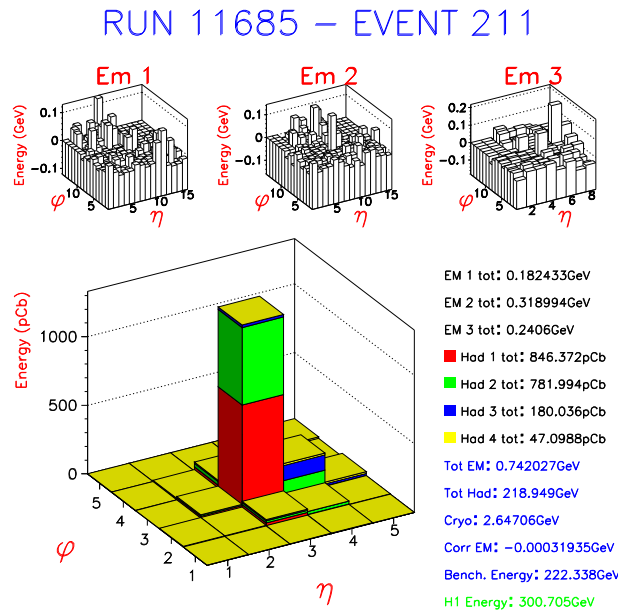Figure 12: Display of an event which is a m.i.p. in the EM calorimeter.
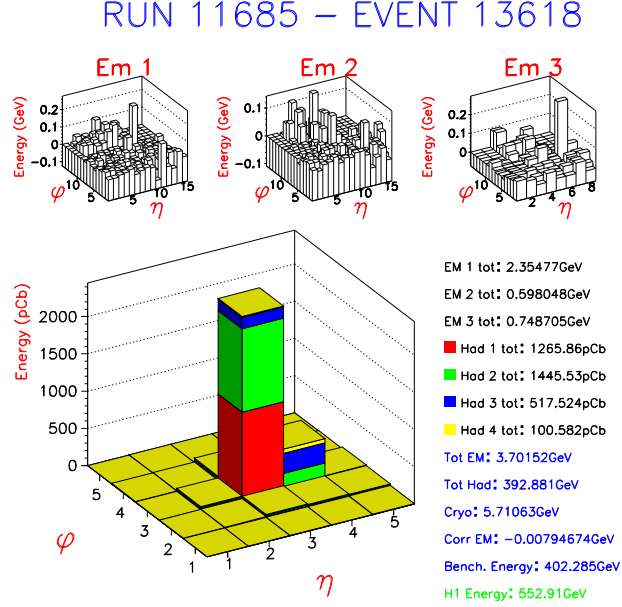
Figure 13: Display of an event which has a benchmark reconstructed energy of 403 GeV, more than 4 σ away from the mean value. The top lego plots show the energy released in the three EM compartments, while the bottom one has the energy released in the four hadronic sections.
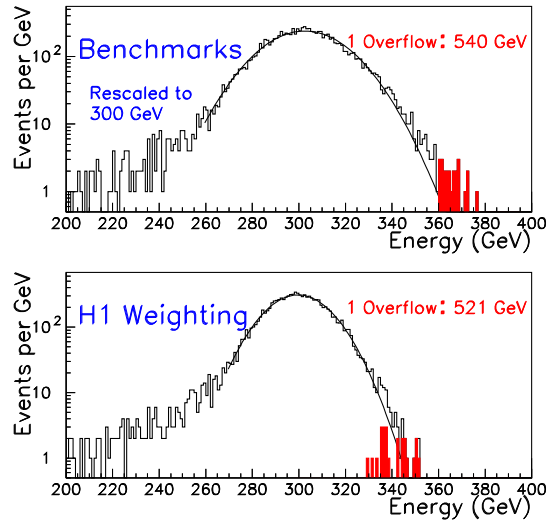
Figure 14: Energy spectra for 300 GeV pions reconstructed with the benchmark technique (plot above) as well as with the H1 technique (plot below).

Table 5 and figure 15(b) show the energy loss due to leakage averaged over punchthrough events (defined as the difference between the mean gaussian energy values of the events with and without a signal in the muon wall) for all the beam energies above 40 GeV. The values observed in 1994 are plotted as well. The 1996 results reproduce very well the ones obtained in 1994 (inside the errors). The energy loss for events with longitudinal leakage is about 3% at 100 GeV, and less than 2.5% at 300 GeV.

18

Beam energy	P_{punch} 94 (%)	$Acc.$ 94	P_{punch} 96 (%)	$Acc.$ 96
40	—	—	3.85	0.51
50	5.51	0.45	4.68	0.51
80	—	—	8.63	0.51
100	15.3	0.44	10.9	0.53
150	—	—	16.9	0.53
200	32.3	0.47	—	—
300	44.5	0.49	38.2	0.53

Table 4: Punchthrough probability (P_{punch}) for the 1994 and 1996 combined test beams. P_{punch} is corrected for the μ wall acceptance, also shown in the third and fifth columns.
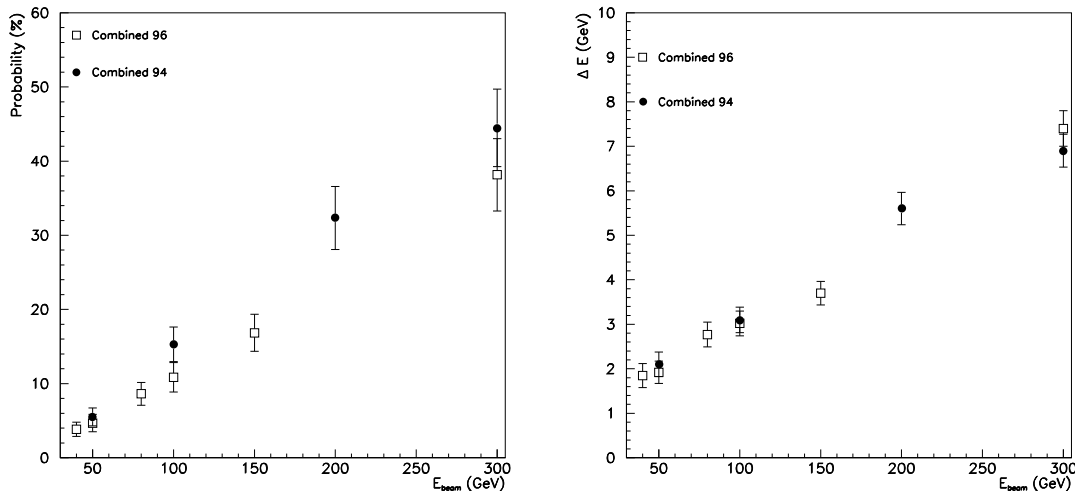

Figure 15: (a) Punchthrough probability for pions. Results from the 1994 combined test beam are shown as well. (b) Average energy loss vs. beam energy for events with longitudinal leakage.

3.5 Evaluation of e/h Ratio

The ratio of the responses obtained for electrons and pions (e/π ratio) gives the possibility to extract the e/h value, that is the ratio of the combined prototypes response to the electromagnetic and non-electromagnetic (purely hadronic) components of the hadron showers. An e/h value different from 1 causes deviation from linearity in the response vs. energy, besides broadening the energy resolution and introducing tails in the energy distribution.

3.5.1 Response to Electrons

Electrons were reconstructed in the EM calorimeter for two purposes, to estimate the electron response in the EM section for the evaluation of the e/h ratio and to measure the energy resolution and linearity in order to verify the quality of the response. To separate electrons from muons and hadrons, cuts were applied demanding a signal in the EM calorimeter compatible with electrons. Furthermore, similar cuts as described in section 3.1 on beam direction and beam position measured by the beam chambers were used together with cuts on the time sum from the delay line readout of the beam chambers and the scintillator pulse height to avoid electrons that have interacted upstreams. Contrary to the pion analysis, no cut was made to restrict the difference on the particle position measured by the calorimeter/presampler system and the beam chambers in order to not bias the energy resolution by cutting late or early shower development.

Beam energy	ΔE 94 (GeV)	ΔE 96 (GeV)
40	—	1.85
50	2.1	1.92
80	—	2.77
100	3.1	3.02
150	—	3.70
200	5.6	—
300	6.9	7.40

Table 5: Mean (gaussian) energy loss for events with leakage.

3.5.2   Reconstruction of Electron Energy

To reduce the noise, the smallest possible cluster (normally 3x3 cells in η, ϕ) must be used. In the present case, however, due to the non-pointing setup of the beam, the energy leakage at the η cluster boundary, would depend on the longitudinal development of the shower as well as the η coordinate. For this reason a 7x3 cell cluster was used.

For 287 GeV electrons the EM response was observed to decrease with increasing signal in the last sampling. A similar decrease was seen in Monte Carlo simulations. This is interpreted as due to longitudinal leakage and corrected for by multiplying the signal from the last sampling with a fitted factor. Furthermore, a multiplicative factor for the presampler signal was obtained by optimizing the energy resolution.

The η and ϕ dependence of the response (beam chamber cuts not applied) are shown in figure 16 and 17 respectively. Both coordinates are expressed in EM calorimeter cell numbers as measured in the first sampling. The η variation of the response is small as expected while the ϕ response reflects the accordion structure as well as losses due to the limited cluster size. The lower response for $\phi > 6.8$ is due to losses in the gap between the modules at $\phi \sim 8.5$. Events where the measured ϕ coordinate was > 6.8 were removed. Corrections for the measured position dependence were applied for each beam energy.
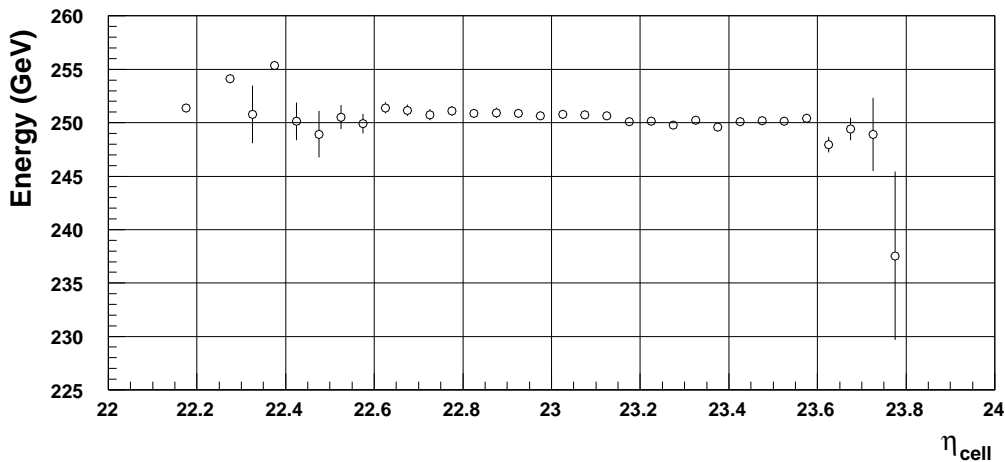

Figure 16: Variation of the energy response with η.

3.5.3   Electron Energy Resolution

Figure 18 shows the measured energy spectrum for electrons at a beam energy of 287.5 GeV.

The obtained energy resolution, corrected for a beam momentum spread of 0.3%, is displayed as a function of beam energy in figure 19. The fitted energy resolution is:
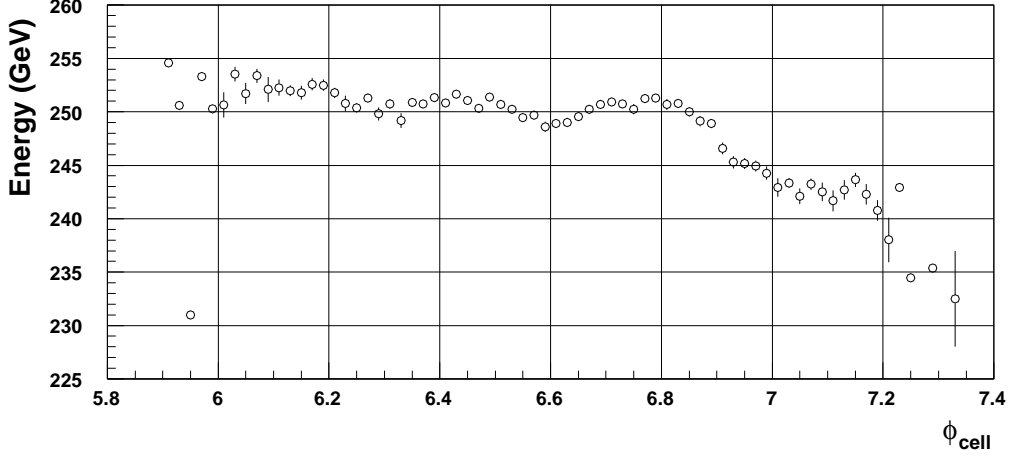
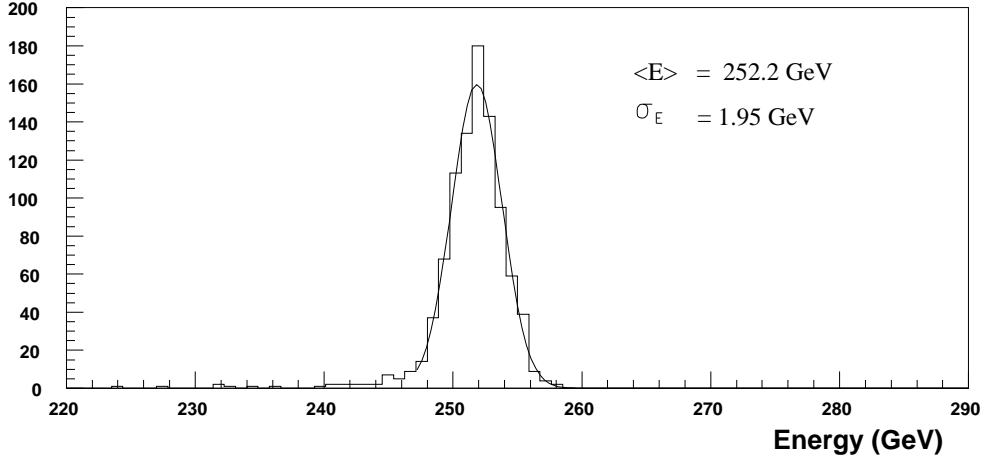Figure 17: Variation of the energy response with ϕ.

Figure 18: The measured energy spectrum for electrons at a nominal energy of 287.5 GeV.

$$\frac{\sigma_E}{E} = \frac{12.15 \pm 0.23\%}{\sqrt{E}} \oplus 0.0 \pm 0.20\% \oplus \frac{374 \pm 54 MeV}{E} \quad (8)$$

The fitted noise term, 374±54 MeV, is slightly larger than the 295±0.1 MeV measured for pedestal triggers at 20 GeV in a 7x3 cluster. The resolution is worse than previously reported in [2] ($9.99\pm0.29/\sqrt{E}\oplus0.35\pm0.04$ %) especially at low energies. This is assumed due to the fact that for the high gain channels of the cells in the 7x3 cluster, only a limited number of valid calibration amplitudes before saturation was available. This did not allow a sufficient precision in the linearization of the response. By assuming a 0.3 % constant term, a fit to the energy resolution gives a sampling term of $11.13 \pm 0.26\%/\sqrt{E}$. Only using the 287.5 GeV electron data results in a sampling term of 10.97%.

3.5.4 Response Linearity

The linearity of the response in a 7x3 cell EM cluster after corrections for longitudinal leakage, signal in the presampler and η and ϕ modulation is shown in figure 20, where the ratio is set to 1 at 150 GeV. The average response to electrons in 11x11 cell clusters, which is the size used for the pion analysis, was also measured removing events where $\phi_{cell} > 6.8$ (not applying any position dependent corrections).
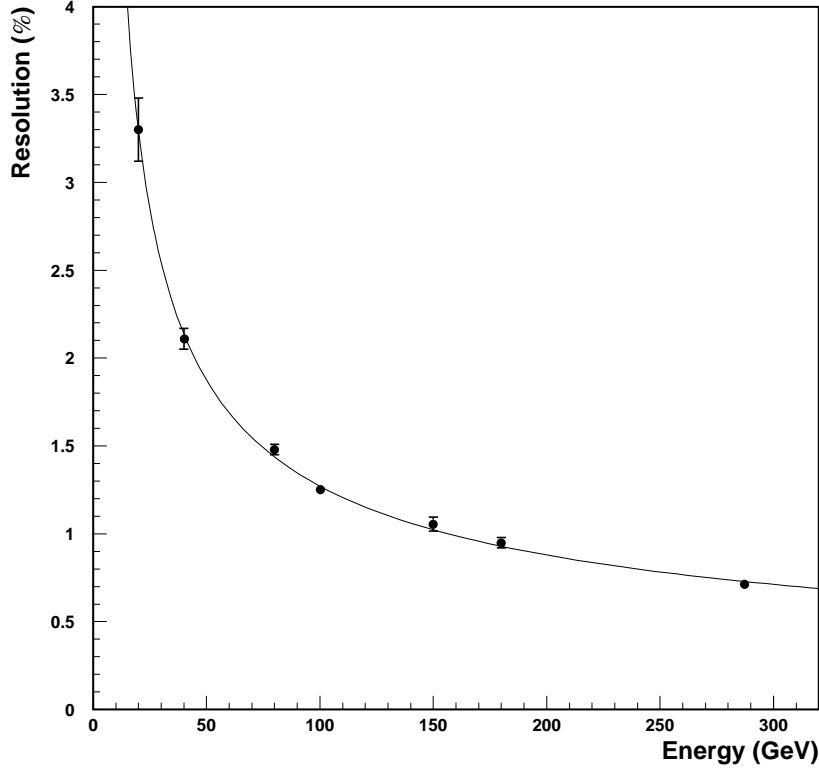
21

Figure 19: The measured energy resolution for electrons in the EM calorimeter. The curve shows the fitted resolution $\frac{\sigma_E}{E} = \frac{12.15 \pm 0.23\%}{\sqrt{E}} \oplus 0.0 \pm 0.20\% \oplus \frac{374 \pm 54 MeV}{E}$.

The average measured energies for both cluster sizes are listed in table 6. The error quoted for the 7x3 cluster is dominated by an estimate of the beam rectifier stability $(4.5\%/P)$ compared to the statistical error on the average measured energy[2]. For the 11x11 cluster, it is assumed that the energy response is a gaussian distribution with a certain average at each impact point in ϕ, where the average depends on ϕ. The R.M.S. of this variation is used as an estimate of the uncertainty of the energy response and given as the error to the average energy response using 11x11 cell clusters. The two dashed lines in figure 20 shows the uncertainty on the nominal beam momentum given as

$$\frac{\Delta(P)}{P} = \frac{25\%}{P} \oplus 0.5\%, \tag{9}$$

where P is in GeV. The first term is related to hysteresis effects in the bending magnets, while the second term reflects calibration and geometrical uncertainties. The linearity is, except at 40 GeV, within errors better than 1%. Deviations can, as previously mentioned, be explained by too few available calibration amplitudes for the high gain channels.

3.5.5 The e/π Ratio

To calculate the e/π ratio for the combined calorimeter system, the knowledge of the absolute energy scale for each calorimeter is needed. For electrons, the signal from the LAr calorimeter is enough to reconstruct their energy. The e/π ratio is therefore defined using the following

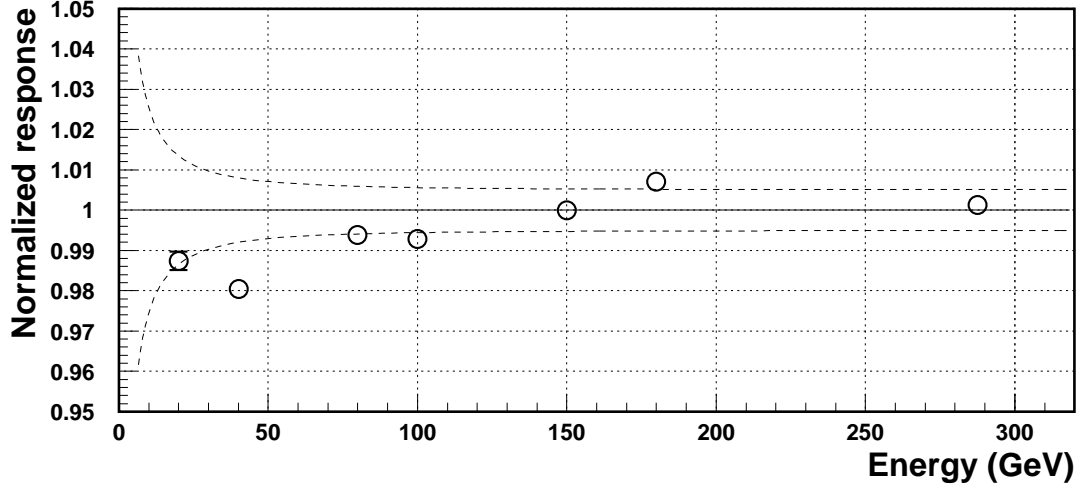---

[2]P is the beam momentum.

22

Figure 20: The ratio of measured to nominal electron energy for 7x3 cell clusters. Error bars and the dashed lines are explained in the text.

Beam Energy	E_{meas} in 7x3 cells	$E_{7x3}/E_{nominal}$	E_{meas} in 11x11 cells	$E_{11x11}/E_{nominal}$
20	17.30±0.03	0.8650±0.0016	18.78±0.23	0.939±0.012
40	34.35±0.02	0.8588±0.0004	36.58±0.15	0.914±0.004
80	69.64±0.02	0.8705±0.0002	73.88±0.21	0.924±0.003
100	86.98±0.05	0.8698±0.0005	91.92±0.35	0.919±0.004
150	131.4±0.04	0.8760±0.0003	138.6±0.47	0.928±0.003
180	160.0±0.04	0.8889±0.0002	167.9±0.58	0.933±0.003
287.5	252.2±0.04	0.8772±0.0001	265.5±0.90	0.923±0.003

Table 6: Energy measured in 7x3 and 11x11 clusters for different nominal electron energies. The errors include a 4.5%/P estimate of the beam rectifier stability which is the dominating source compared to the statistical error used for the 7x3 cluster. For the 11x11 cluster, the errors reflects the response variation in ϕ (see text). The ratios of the measured to nominal energies for the two cluster sizes are also listed.

formula:

$$\frac{e}{\pi} = \frac{< e_{LAr}E_{em}^e >}{< e_{LAr}E_{em}^\pi + e_{Tile}E_h^\pi + E_{cryo}^\pi >} \,, \tag{10}$$

The expression used in the denominator is similar to the benchmark formula defined in section 3.3.1, but without the quadratic correction factor. E_{em}^e and E_{em}^π are the response of the LAr calorimeter to electrons and pions, E_h^π is the response of the Tilecal calorimeter to pions and E_{cryo}^π is the energy loss in the cryostat. The two constants $e_{LAr} = 1.1$ and $e_{Tile} = 0.145\text{GeV/PCb}$ are calibration constants needed to achieve the correct electron energy scale in LAr and Tilecal calorimeters[3].

For the case of stand-alone calorimeter that formula leads us to the obvious expression $e/\pi = E^e/E^\pi$. The e/π ratios for beam energies between 20 and 300 GeV are listed in table 7.

For the 300 GeV energy point an offset of 12.5 GeV was added to the reconstructed mean energy of the 287.5 GeV electrons. An additional error for the 20 GeV point of 2% was introduced

---

[3]The constant e_{Tile} cannot be directly measured as the direct response to electrons cannot be studied. Anyway the response of the Tilecal calorimeter to pions can be obtained by selecting m.i.p. in the three LAr samplings. From this calibration constant to pions we can extract e_{Tile} by dividing for the $(e/\pi)_{Tile}$ measured in a stand-alone test beam.

E_{beam} (GeV)	e/π ratio
300	1.114 ± 0.013
150	1.137 ± 0.013
100	1.158 ± 0.012
80	1.170 ± 0.013
50	1.174 ± 0.012
40	1.186 ± 0.012
20	1.278 ± 0.016

Table 7: e/π ratio for the various beam energy.

due to the large uncertainty in the electron definition (beam spot in $6.5 < \phi < 7.2$). The e/h ratio was extracted by fitting the data with the expression:

$$\frac{e}{\pi} = \frac{e/h}{1 + (e/h - 1) \ 0.11 \ lnE} \ .$$

(11)

Figure 21 shows the e/π ratios for the 1996 combined data (black circles) and for the 1994 combined data (open circles). The solid curve is a fit performed with function (11). As a result
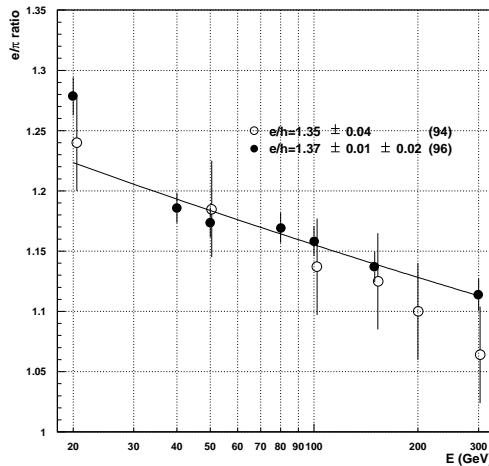
Figure 21: Distribution of the e/π ratio versus the beam energy, fitted by the expression (11). Black circles show the results for the combined 1996 setup. The open circles are the results for the combined 1994 setup.

we get $e/h = 1.37 \pm 0.01 \pm 0.02$, which is in good agreement with the value obtained in 1994 ($e/h = 1.35 \pm 0.04$).

3.6   Angular resolution

The data collected was also used to determine the angular resolution of hadronic showers. This is of interest since, for istance, the knowledge of the direction of the decay jets can be useful to improve the mass reconstruction of particles decaying into pair of jets. The polar angle reconstruction was studied with 1994 data too [11].

In addition to the cuts described in section 3.3.1 the following one was applied:

$$\left| E_{tot} - \overline{E_{tot}} \right| < 3 \times \sigma_E$$

(12)

24

Where $\overline{E_{tot}}$ and σ_E are taken from the gaussian fit to the reconstructed energy distribution for each beam energy. The energy is reconstructed using the benchmarck technique.

A threshold cut of *0 GeV* was applied to all the cells in both calorimeters. For this study, the cells in the the fourth longitudinal hadronic sampling were not used, as they have small deposited energy.

3.6.1 Polar angular resolution

The polar angle (θ) is reconstructed in the following way: for each longitudinal sampling (i), the center of gravity along the horizontal axis (x_{CG}^i) in the plane of the front face of the calorimeter, is determined, on an event by event basis:

$$x_{CG}^i = \frac{\sum_{j,k} E_{j,k}^i \cdot x_k^i}{\sum_{j,k} E_{j,k}^i} \tag{13}$$

In the plane of the calorimeter front face, the k index runs along the horizontal axis x, and the j index runs along the vertical axis y (or angle ϕ). Therefore, $E_{j,k}^i$ is the energy deposited in cell (j,k) of the ith longitudinal sampling, and x_k^i is the x central position of the kth cell in the horizontal axis. Since the electromagnetic compartment has a projective geometry (η cells), the cell center positions are first converted from η values (in rad) to x values (in cm).

Once the x_{CG}^i are obtained, a fit is performed with the function:

$$z^i = tan(\theta) \cdot x_{CG}^i + b \tag{14}$$

event by event, where z^i is the ith longitudinal sampling center position (along the radial (z) axis), to extract the parameter $tan(\theta)$.

Figure 22 shows the x_{CG}^i distributions for the 3 EM and 3 had longitudinal samplings. Those distributions refer to 300 GeV pions.

The polar angle distribution for 300 GeV pions is shown in figure 23. The mean $\overline{\theta} = 11.91^o$, and the resolution $\sigma_\theta = 0.94^o$ are obtained from a gaussian fit in the $\pm 2 \cdot \sigma$ range around $\overline{\theta}$.

The method previously described was applied to all beam energies (20 GeV to 300 GeV), thus obtaining $\overline{\theta}$ as a function of energy as shown in figure 24 on the right.

Averaging θ over the whole energy range gives:

$$< \theta > = (11.87 \pm 0.09)^o \tag{15}$$

This value is consistent with the nominal value stated previously. The angular resolution is well parametrized by the function:

$$\sigma_\theta = \left(\frac{160.50 \pm 1.48}{\sqrt{E}} + 8.15 \pm 0.20 \right) mrad \tag{16}$$

In table 8 is given for each beam energy, the mean value $\overline{\theta}$ (in ^{o}) and σ_θ (in $mrad$), taken from a gaussian fit to the distribution of the reconstructed the polar angle.

Figure 24 shows σ_θ as a function of $1/\sqrt{E}$ (on the left).

The method applied in 1994 to reconstruct polar angle [11] was also used and the results obtained are reported as well.

3.6.2 Azimuthal angular resolution

The azimuthal angle (ϕ) is reconstructed for each longitudinal sampling (i) and each event with the formula:

$$\phi_{CG}^i = \frac{\sum_{j,k} E_{j,k}^i \cdot \phi_j^i}{\sum_{j,k} E_{j,k}^i} \tag{17}$$

Figure 22: Distribution of the x center of gravity for each longitudinal sampling, determined in an event by event basis, for 300 GeV π's. On the left are the three EM samplings, and on the right the three HAD samplings. Tails in the figure are due to finite granularity of the calorimeters.
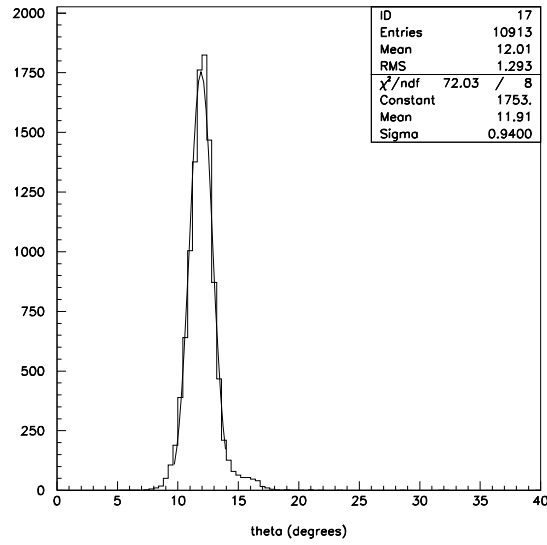
Figure 23: Polar angle (θ) distribution, from an event by event fit to eq. 14, for 300 GeV pions.

Beam Energy	$\theta\ (^o)$	$\sigma_\theta\ (mrad)$	$\theta\ (^o)$ note 70	$\sigma_\theta\ (mrad)$ note 70
20	11.67 ± 0.035	43.73 ± 0.62	11.58 ± 0.12	43.97 ± 1.26
40	11.88 ± 0.032	33.21 ± 0.53	11.72 ± 0.08	34.19 ± 1.31
50	11.85 ± 0.030	30.89 ± 0.49	11.81 ± 0.10	29.78 ± 0.73
80	11.87 ± 0.024	27.16 ± 0.40	11.50 ± 0.06	25.81 ± 0.78
100	11.94 ± 0.022	24.68 ± 0.35	11.69 ± 0.05	23.62 ± 0.79
150	11.97 ± 0.017	21.31 ± 0.28	11.78 ± 0.03	20.18 ± 0.49
300	11.91 ± 0.010	16.41 ± 0.17	11.91 ± 0.03	15.36 ± 0.39

Table 8: Mean value $\overline{\theta}$ and σ_θ for each beam energy using the method proposed in note 70 and the new method.
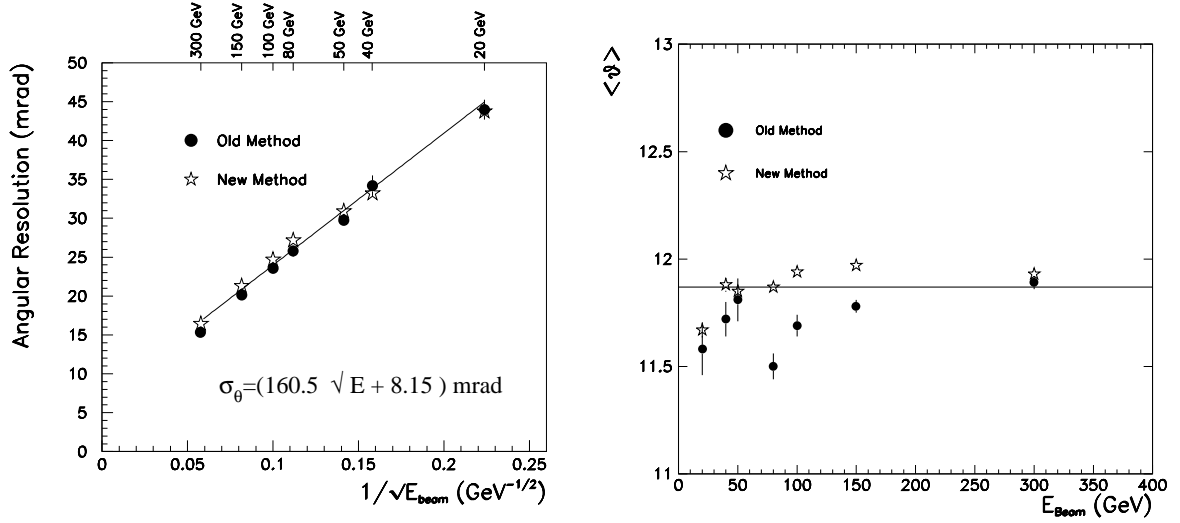
Figure 24: Left: Polar angular resolution, σ_θ as a function of $1/\sqrt{E}$. Right: Mean polar angle ($\overline{\theta}$ in degrees) as a function of beam energy.

As in equation 13, k runs over the horizontal axis, and j runs along the vertical axis. As previously stated, the EM segmentation in ϕ is 0.02 rad while the hadronic segmentation is of 0.1 rad. The beam hits the calorimeter at $\phi = 0$.

Figure 25 shows ϕ^i_{CG} for the three EM and three HAD longitudinal samplings, for 300 GeV π's.

For each event the average of the 6 values of ϕ^i_{CG}, is calculated, figure 26 shows the 300 GeV π's case.

Table 9 shows for each beam energy, the mean value $\overline{\phi}$ and the width of the distribution σ_ϕ taken from a gaussian fit to the reconstructed ϕ distribution. As expected $\overline{\phi}$ peaks around 0 rad. Figure 27 shows σ_ϕ as a function of $1/\sqrt{E}$, parametrized with the function:

$$\sigma_\phi = \left(\frac{68.17 \pm 0.75}{\sqrt{E}} + 0.91 \pm 0.11 \right) mrad \qquad (18)$$

3.7 Longitudinal energy deposition.

To study the longitudinal shower energy deposition in both calorimeters, we applied in addition to the standard cuts used in Section 3.1, the following ones:

- $E_{Beam} = 80 \div 300$ GeV: $E_{bench} > 10$ GeV
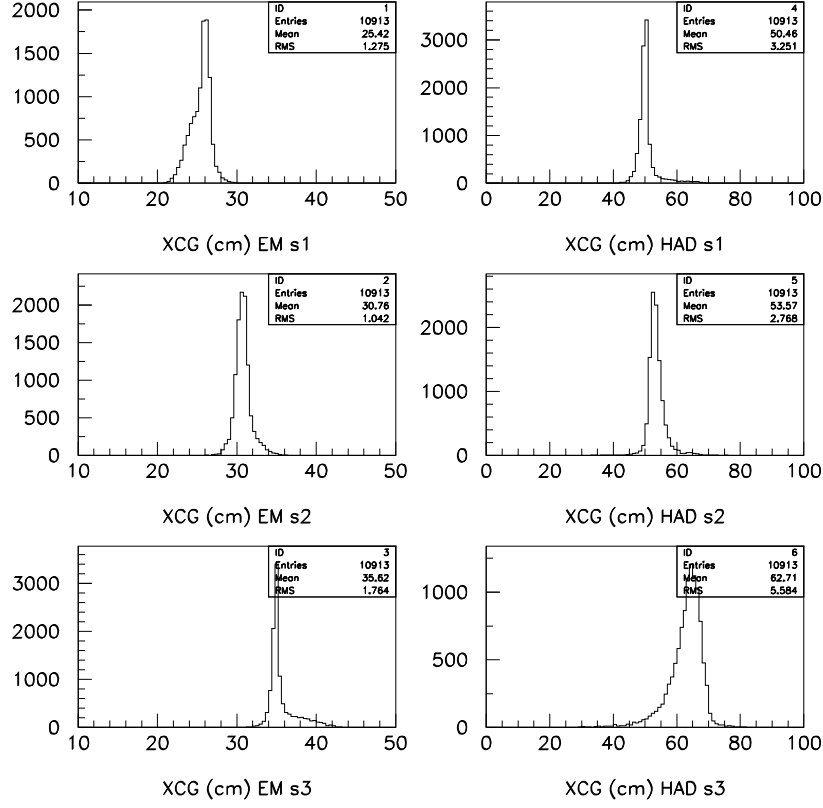
27
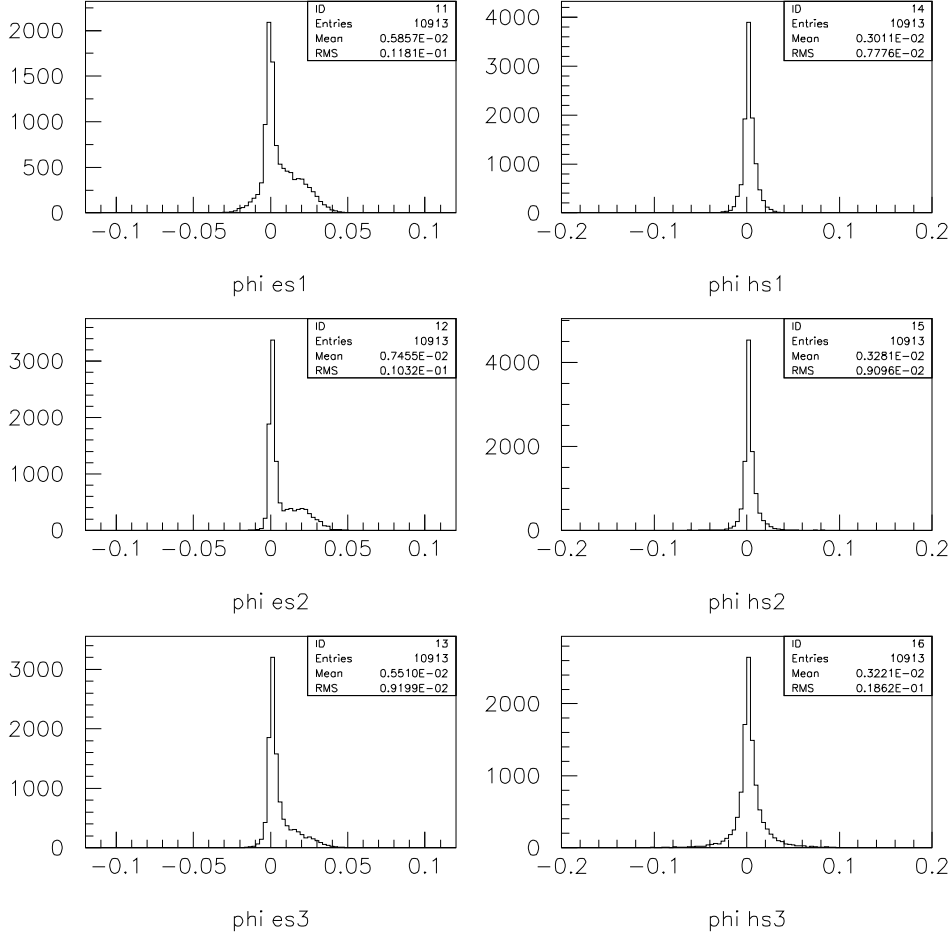
Figure 25: Distribution of the ϕ center of gravity for each longitudinal sampling, determined on an event by event basis, for 300 GeV π's. On the left are the three EM samplings, and on the right the three hadronic samplings.

- $E_{Beam} = 50$ GeV: $E_{bench} > 6$ GeV

- $E_{Beam} = 40$ GeV: $E_{bench} > 4$ GeV and $tbeamsc3 < 73$

- $E_{Beam} = 20$ GeV: $mumod1 + mumod2 < 10$

- $E_{Beam} = 10$ GeV: $mumod1 + mumod2 < 5$

With E_{bench} the total energy reconstructed using the benchmark technique (see Section 3.3.1), $mumod1$ and $mumod2$ the energy released in the two muon walls, and $tbeamsc3$ energy released in a scintillator after the beam dump.

The mean raw energy deposited in each sampling can be plotted against the calorimeter depth to give a useful representation of the shower longitudinal development. Figure 28 shows the longitudinal energy deposition for pions of 50 and 300 GeV compared with the 1994 combined test beam data.

The energy deposited in the electromagnetic compartment is divided by 0.923, since the EM calorimeter is only detecting 92.3% of the energy (see section 3.5). For the Tilecal calorimeter we chose a calibration constant 0.145 as described in section 3.5.5.
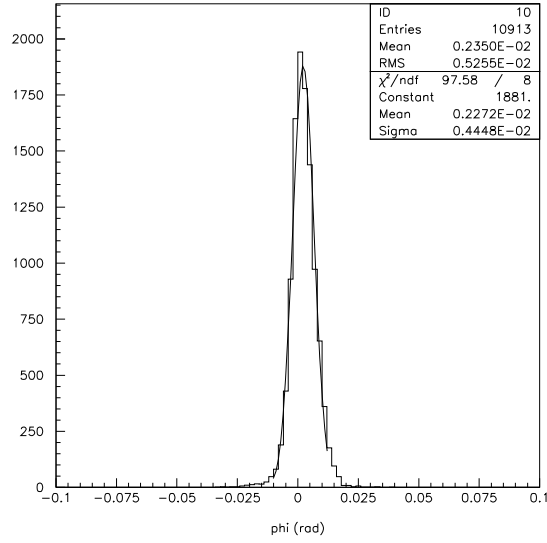
Figure 26: Azimuthal angle (ϕ) distribution for 300 GeV pions.

Beam Energy	$\phi \ (mrad)$	$\sigma_\phi \ (mrad)$
20	2.55 ± 0.21	16.15 ± 0.21
40	1.17 ± 0.18	11.77 ± 0.18
50	0.46 ± 0.17	10.25 ± 0.16
80	0.08 ± 0.13	8.52 ± 0.13
100	0.73 ± 0.12	7.80 ± 0.11
150	1.78 ± 0.09	7.01 ± 0.08
300	2.24 ± 0.05	4.45 ± 0.04

Table 9: Mean value $\overline{\phi}$ and σ_ϕ for each beam energy.

It can be seen that in the hadronic compartment, the 1996 data agrees very well with the 1994 test beam data. For the EM compartment, a slightly smoother profile is observed for 300 GeV in 1996 data, than in the previous test beam.

The longitudinal shower development has been calculated by normalizing the FLUKA response at 300 GeV to the experimental one. They both depend on the parameter set used, but, as shown in figure 29, the experimental longitudinal development is well reproduced. Figure 30 shows the percentage of the total raw energy released in the electromagnetic and hadronic calorimeter for different beam energies. For all the energy range, ∼50% or more of the energy is deposited in the hadronic calorimeter. The 1996 data results agree rather well with the 1994 ones.
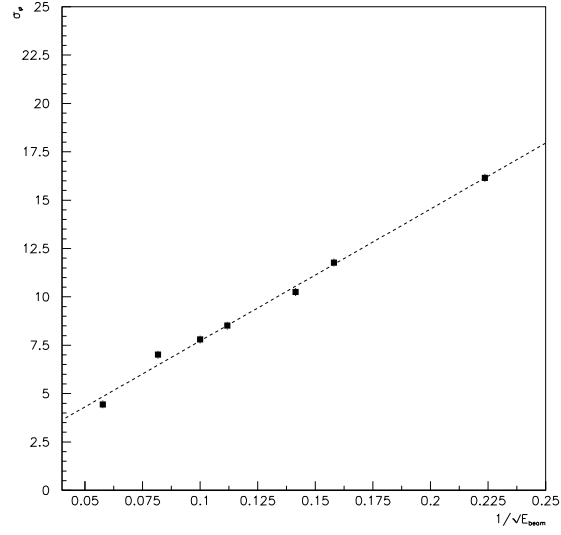
Figure 27: Azimuthal angular resolution, σ_ϕ as a function of $1/\sqrt{E}$.

Sampl.	50 GeV (94)	50 GeV (96)	300 GeV (94)	300 GeV (96)
EMS1	4.40	4.29	16.05	16.96
EMS2	5.94	5.24	32.55	28.38
EMS3	3.48	3.22	18.90	19.08
HADS1	11.41	11.67	67.47	71.21
HADS2	9.72	9.65	70.23	72.93
HADS3	4.05	3.62	36.27	34.26
HADS4	1.15	0.94	13.23	12.13

Table 10: Energy deposition in each sampling of the EM and HAD calorimeters, for 50 and 300 GeV pions. The results are listed for the 1994 and 1996 test beam data.

Beam energy	HAD (94) (%)	EM (94) (%)	HAD (96) (%)	EM (96) (%)
10	—	—	52.73	47.27
20	56.8	43.2	59.14	40.86
40	—	—	65.34	34.66
50	66.0	34.0	66.99	33.01
80	—	—	68.69	31.31
100	68.9	31.1	69.78	30.22
150	72.0	28.0	72.16	27.84
300	73.1	26.9	74.71	25.29

Table 11: Percentage of energy deposition in the EM and HAD calorimeters, for all pion energies. Comparison of 1994 and 1996 data.
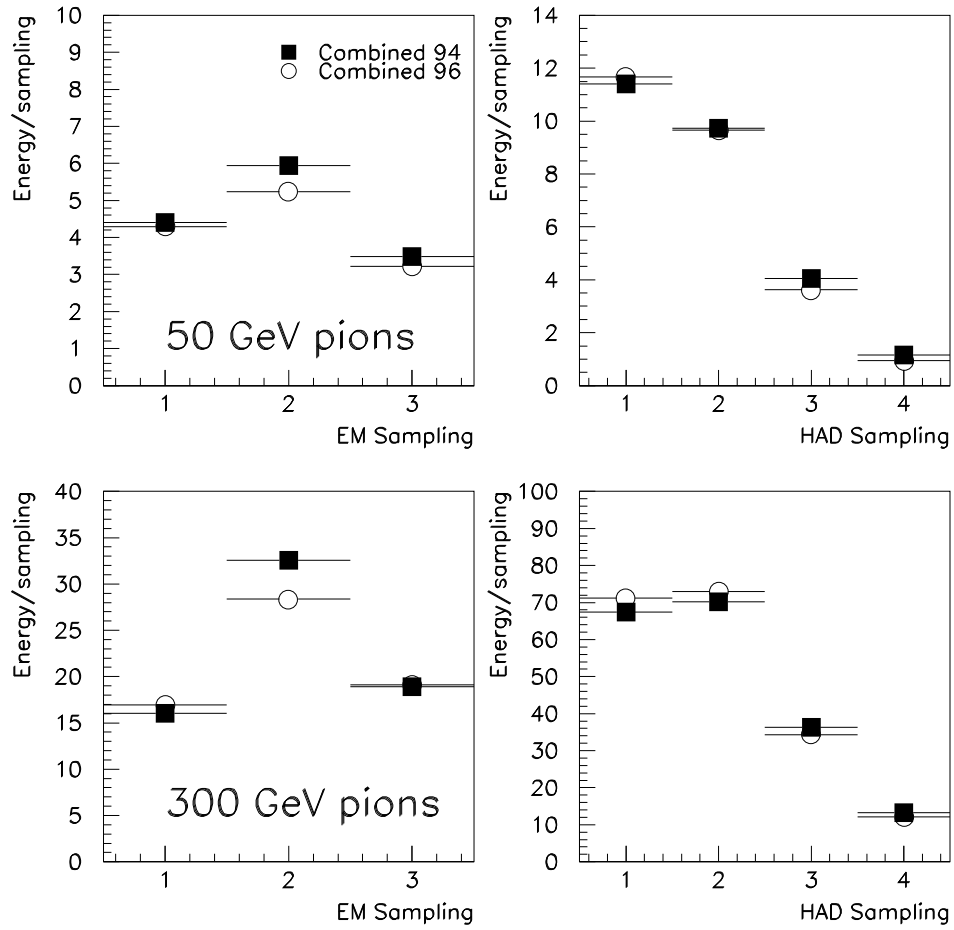
Figure 28: Energy deposition in each sampling of the EM (on the left) and hadronic (on the right) calorimeters for pions of 50 (on top) and 300 GeV (on bottom). The data are compared with 1994 test beam data.
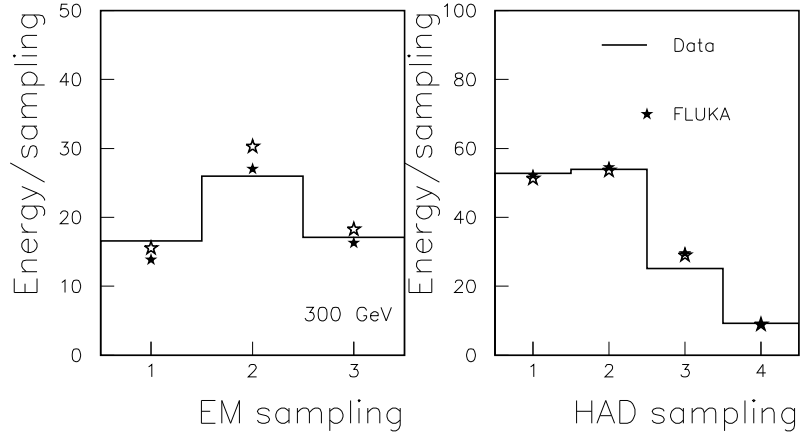
Figure 29: Longitudinal shower development for 300 GeV pions. The close stars refer to parameter set A , the open stars to parameter set B. Set A and set B have been defined in Section 3.3.1.
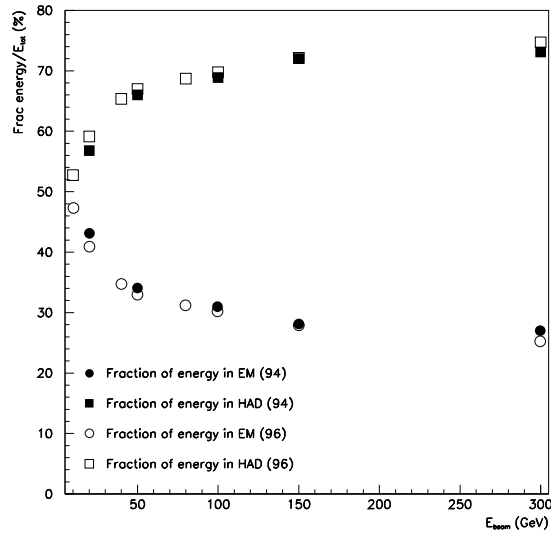
Figure 30: Energy deposition (percentage) in the electromagnetic and hadronic calorimeters for the 1996 and the 1994 data, at different beam energies.

4   Muon Response

The combined calorimeter response to muons has been investigated for several incident energies (20 to 150 GeV). The reconstruction of a muon signal is important since it can be used e.g. for b-tagging; isolated muons provide an evidence for several processes of interest and they can be used for detector intercalibration as well.

Muons were extracted from the pion beams. The muon signal is small, so the noise must be treated carefully. The algorithms used are described below. The absolute energy scale was set up using 100 GeV electrons in the electromagnetic calorimeter, while in Tilecal 100 GeV pions have been used, taking into account the e/π ratio (see [21]).

4.1   Muon Response in the Electromagnetic Calorimeter

The muon signal is reconstructed summing up two cells in each longitudinal sampling. First, the central cell is selected using the projection of the muon track from the beam chambers. After that, the maximum signal cell is searched for in between the eight cells adjacent to the central one.

The signal distribution has been fitted with the Landau⊗Gauss convolution [22]. The obtained most probable (MOP) values and the respective full widths at half maximum (FWHM) are listed in table 12.

The following procedure has been used to estimate the noise. First, the noise distribution has been evaluated in each channel separately. As the muon signal is formed summing up a pair of channels which can vary event by event, the corresponding noise has been treated as the noise sum of the respective pair of channels keeping the same proportion of readout cells.

The signal-to-background ratio defined as:

$$S/B = \frac{MOP}{\sigma_{\text{noise}}} \tag{19}$$

for the total LAr response is listed in table 12 as well. The electromagnetic calorimeter response

E_{beam} (GeV)	Total signal		Total noise	S/B
	MOP (GeV)	FWHM (GeV)	σ_{noise} (GeV)	
20	0.39	0.16	0.045	8.8
40	0.37	0.15	0.043	8.6
50	0.36	0.16	0.043	8.4
80	0.38	0.16	0.045	8.5
100	0.38	0.17	0.044	8.5
150	0.37	0.18	0.044	8.5

Table 12: Total LAr calorimeter response to muons. The MOP and FWHM values were obtained using the Landau⊗Gauss convolution fit.

to 150 GeV muons together with the noise distribution is shown in figure 31.

4.2   Muon Response in Tilecal Calorimeter

In order to avoid summing up cells without signal, only the central modules (2,3,4) are used since the beam hits the centre of the prototype module 3 in the ϕ direction. Furthermore, in each longitudinal sampling, a cell with the maximum average signal is taken as a central one, since it corresponds to the cell where the beam is supposed to enter. The central cells always belongs to module 3. The other cells are then searched for in the 3×3 cells window around the central cell.

The muon signal in the hadron calorimeter has been reconstructed summing two cells from the 3×3 window with maximum signal content in each longitudinal sampling[4]. The noise has been treated in the same way as in the case of the electromagnetic calorimeter.

The muon signal distribution is fitted with the Landau⊗Gauss convolution, keeping the Landau parameter ratio $P2$/width fixed at the value obtained with the pure Landau fit to respective simulation results. The most probable (MOP) values of the total muon signal in Tilecal are listed in table 13. The MOP values slightly increase with the incident muon energy.

E_{beam} (GeV)	Experimental data				MC simulation	
	Landau⊗Gauss		Deconvoluted Landau		Pure Landau	
	MOP (GeV)	FWHM (GeV)	Peak (GeV)	Width (GeV)	Peak (GeV)	Width (GeV)
20	2.35	0.83	2.26	0.54	2.48	0.59
40	2.41	0.89	2.32	0.61	2.52	0.67
50	2.44	0.83	2.37	0.64	2.53	0.68
80	2.46	0.93	2.38	0.72	2.58	0.78
100	2.55	1.14	2.44	0.80	2.61	0.85
150	2.66	1.23	2.56	0.97	2.70	1.02

Table 13: Total Tilecal response to muons at various energies. The MOP and FWHM values were obtained with the Landau⊗Gauss convolution fit, the values of peak and width are those from the Landau part of the convolution. The results of the pure Landau fit to the Monte Carlo simulation data are shown for comparison.

The absolute energy scale in the Tilecal standalone simulation data was set up using the signal of 100 GeV electrons averaged over different impact points in one period. Therefore, the peaks and widths obtained when fitting the simulation data with pure Landau function can be compared with the respective peaks and widths from experimental data (obtained from the Landau part of the Landau⊗Gauss convolution). The Monte Carlo simulations result in a signal which is about 10% higher if compared to experimental data (see table 13).

The last Tilecal longitudinal sampling is important for a possible detection of the non-isolated low energy muons, which can be evidence of a B-meson decay. In the real ATLAS setup, the last radial Tilecal depth represents 1.9λ. This corresponds to the second depth ($\approx 1.9\lambda$ as well) of the Tilecal prototype module, therefore the S/B ratio is an important parameter in this compartment. The S/B values of the second sampling and total Tilecal are listed in table 14. The signal from 150 GeV muons in Tilecal as well as the noise distribution are shown in figure 32.

E_{beam} (GeV)	S/B	
	2nd sampling of prototype module	Total Tilecal prototype
20	16.3	35.5
40	16.5	36.8
50	16.4	38.3
80	16.9	38.6
100	16.3	38.3
150	17.2	38.9

Table 14: Signal-to-background ratio (19) for the muon signal at various incident energies. The signal is well separated from the noise.

---

[4]This turns out to be sufficient, because the full sum of 9 cells results in the same (within errors) most probable signal prediction as does the method used, but the full sum peak is wider. However, the method used might underestimate the energy loss for muons emitting bremsstrahlung or electron-positron pairs.

The experimental data can be compared with those from standalone 1996 beam test ($\theta =$ 10 deg) [23]. Here, the Moyal fit is used to determine the MOP values and widths, because the 1996 data were treated in this way. The obtained values are listed in table 15. The results are

E_{beam} (GeV)	Combined beam test		Standalone beam test	
	MOP (GeV)	Width (GeV)	MOP (GeV)	Width (GeV)
20	2.29	0.57	2.28	0.55
50	2.41	0.60	2.40	0.59
100	2.49	0.78	2.51	0.75
150	2.63	0.90	2.61	0.85

Table 15: Comparison of the hadron calorimeter muon response in the combined LAr+Tilecal and standalone Tilecal calorimeter [23] beam tests. Both types of data were treated in the same way, therefore the MOP values and widths are fitted with the Moyal function here.

in good agreement.

4.3 Combined Response

The combined calorimeter response to muons has been fitted with the Landau⊗Gauss convolution as well. Plots with the signal and noise distributions are shown in figure 33 for the lowest and highest incident muon energy studied. The MOP and FWHM values are listed in table 16. The MOP value slowly increases with incident energy, the signal is well separated from the noise.

E_{beam} (GeV)	MOP (GeV)	FWHM (GeV)
20	2.82	0.88
40	2.82	0.86
50	2.87	0.95
80	2.93	0.98
100	3.02	1.22
150	3.06	1.39

Table 16: The combined calorimeter response to muons at various incident energies. The listed MOP and FWHM values were obtained with the Landau⊗Gauss convolution fit.

1.sampling

χ^2/ndf	42.01 / 37
P1	1010.
P2	0.1216
P3	0.1912E-01
P4	0.2411E-01

2.sampling

χ^2/ndf	21.46 / 37
P1	1023.
P2	0.1183
P3	0.1904E-01
P4	0.2256E-01

3.sampling

χ^2/ndf	66.81 / 44
P1	1671.
P2	0.9923E-01
P3	0.1099E-01
P4	0.2673E-01

Total LAr

χ^2/ndf	39.94 / 38
P1	1025.
P2	0.3596
P3	0.4988E-01
P4	0.4690E-01

Dep. E [GeV]

Figure 31: The LAr calorimeter response to 150 GeV muons. Separate samplings as well as the total response are shown. The hatched peaks correspond to noise distribution.
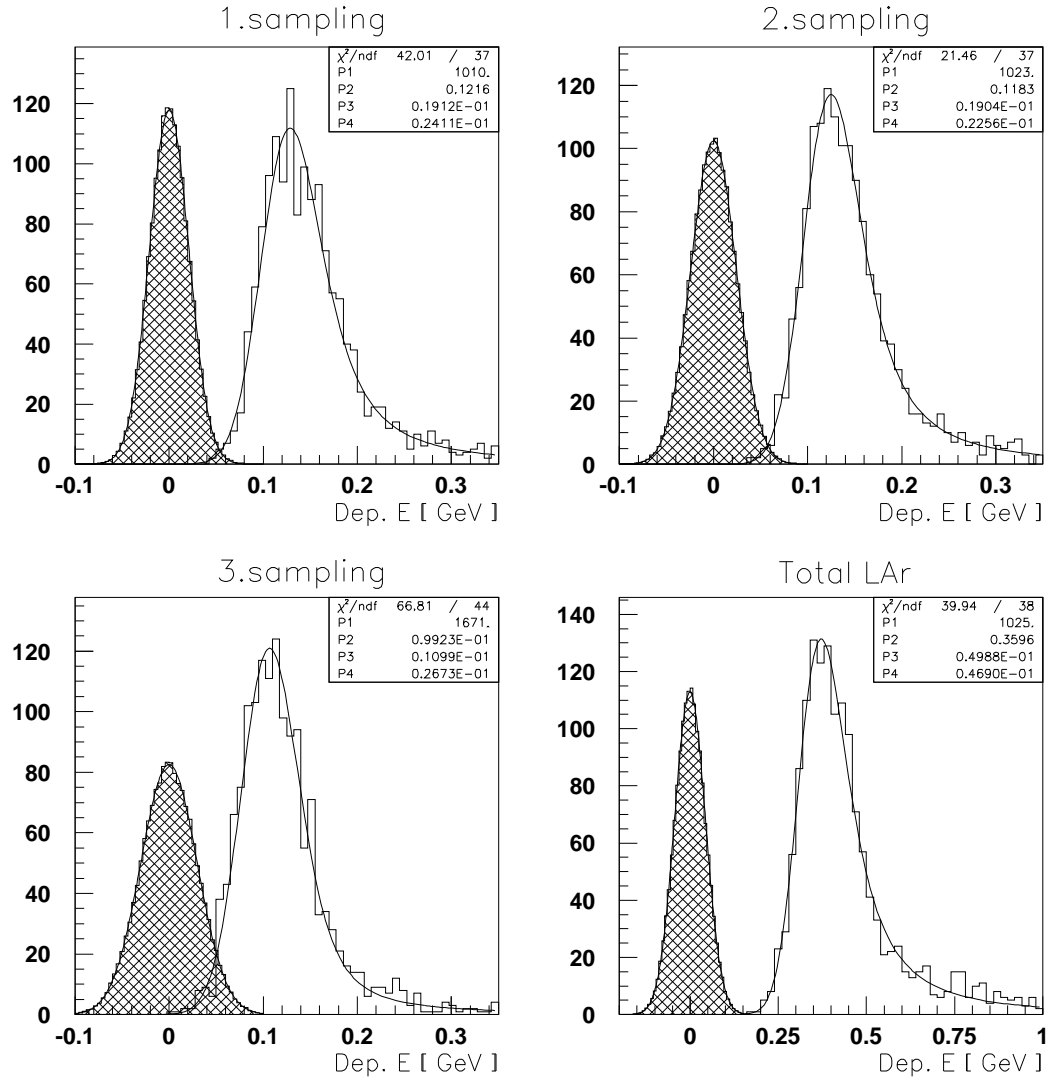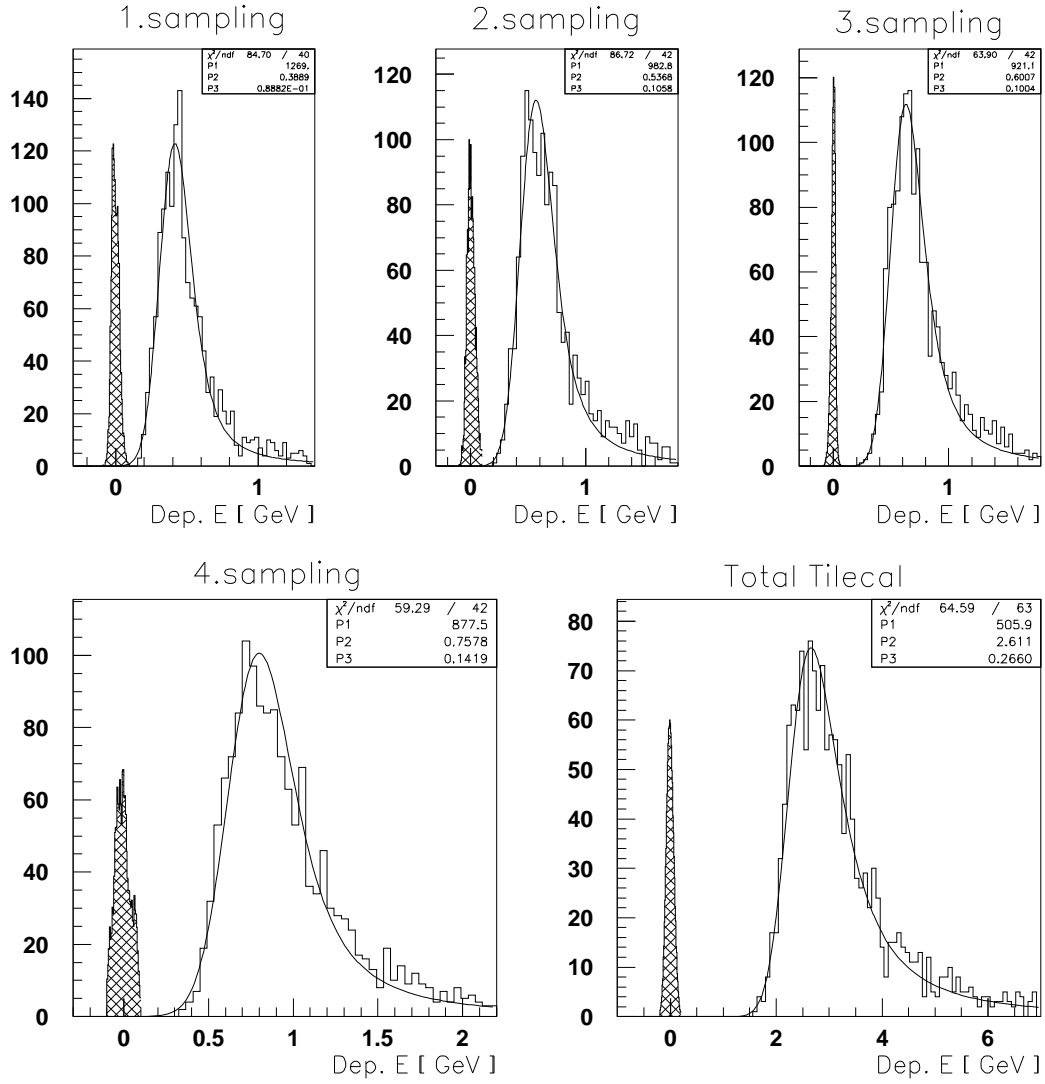
Figure 32: The Tilecal calorimeter response to 150 GeV muons. Separate samplings as well as the total response are shown. The hatched peaks correspond to noise distribution.
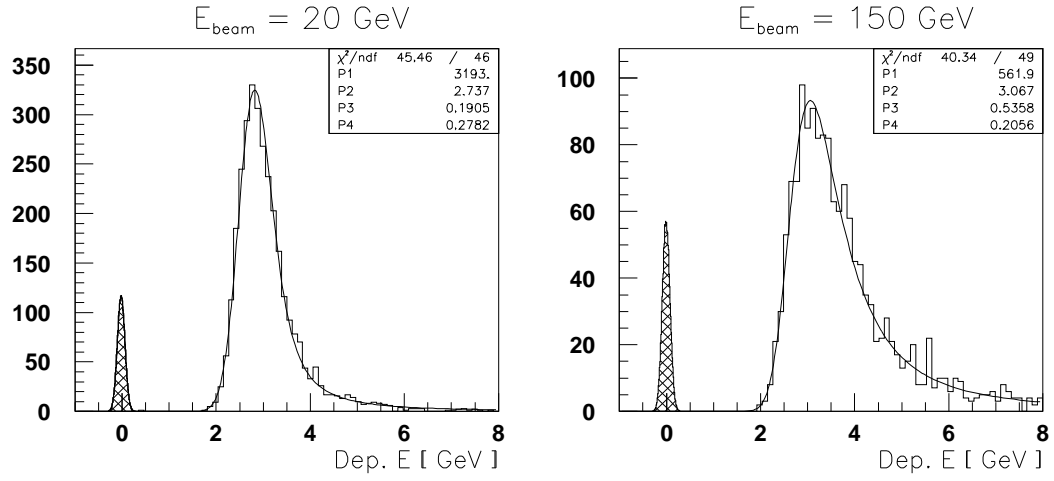
Figure 33: The combined calorimeter response to muons at 20 GeV (left plot) and 150 GeV (right plot). The signal was fit using the Landau⊗Gauss convolution, the hatched area corresponds to noise distribution.

5 Noise evaluation

5.1 General description of the noise

The electronic noise, in the response of each readout channel, affects the calorimeter energy resolution σ/E mainly at low energies, contributing to the 1/E term in the resolution parametrization formula:

$$\frac{\sigma}{E} = (\frac{a}{\sqrt{E}} + b) \oplus \frac{c}{E} \qquad (20)$$

A detailed study was performed to determine the noise level in the combined setup and to get an estimate for the parameter c from eq. (20). To measure the noise we used the events recorded during the pedestal triggers before and after the SPS beam burst. To characterize the noise in a given cell we used the Standard Deviation of the signal recorded in this cell during pedestal events.

When we deal with particle energy reconstruction, we sum over the responses of several adjacent readout cells. To evaluate the noise in this case we have to take into account not only the intrinsic noise produced by each readout channel, but also the noise induced by the mutual influences of the surrounding channels. We describe the noise using two parameters:

- σ_{rnd}, the random noise which is the mean intrinsic noise produced by a single channel;

- σ_{coh}, the coherent noise, which is the mean noise induced in a channel by a cross-talk with other channels.

For the Tilecal calorimeter the analysis was performed module by module as well as on all modules simultaneously. For LAr calorimeter, the analysis was performed per sampling, per type of readout electronics in each sampling and finally per readout type over all samplings.

The two components of the noise contribute differently to the total noise in n channels. A group of n channels produces a total random noise which is given by an incoherent addition of the random values in the individual channels. By hypothesis, the coherent noise is uniformly distributed between calorimetric cells, which implies a linear increase with n of the total coherent noise. The total noise is given by the quadratic addition of the random and coherent components:

$$\sigma_n^2 = n\sigma_{rnd}^2 + n^2\sigma_{coh}^2 \qquad (21)$$

5.2 The Methods

Two techniques were used to estimate the values of random and coherent noise, both of them relying on fits to the dependence on n.

- Method I (standard)

Equ. (21), could be used to fit simultaneously the values of random and coherent noise.

The input data in the fit are the values of σ_n. To obtain them, the distributions of S_n, the cumulated response of n readout cells are built:

$$S_n = \sum_{i=1,n} E_i \qquad (22)$$

for different values of n, where E_i represent the response of the individual calorimetric cells, taken from pedestal events. The values of σ_n are obtained by fitting these distributions with a Gaussian function.

- **Method II**

E_i, the responses of different channels, can be taken with alternate signs:

$$S_n^{\pm} = \sum_{i=1,n} (-1)^i E_i \qquad (23)$$

where n, the total number of readout channels is even. Provided the hypothesis of uniform distribution of coherent noise is correct, the contributions of individual channels to the total coherent noise in $S_n^{\pm}$ should cancel out. This can be used to determine the random noise, by a fit of $\sigma_n^{\pm}$, the standard deviation of $S_n^{\pm}$ distribution. There are two ways to do it:

- to fit $\sigma_n^{\pm}$ with equ. (21), and finding out that the contribution of the coherent component is consistent with zero, a procedure which will allow to check the hypothesis made above on the coherent noise;

- to consider that in $\sigma_n^{\pm}$ only the random noise contributes and fit it with:

$$\sigma_n^{\pm} = \sigma_{rnd} \sqrt{n} \qquad (24)$$

One can notice that fitting the dependence $\sigma_n^{\pm}$ vs. n with equ. (21) or equ. (24), provides an estimate of σ_{rnd} which is independent from that obtained previously using Method I.

Combining σ_n and $\sigma_n^{\pm}$ extracted from the distributions of S_n and $S_n^{\pm}$ it is possible to isolate the contribution of the coherent noise. The value of σ_{coh} could be obtained from a fit, taking into account the coherent noise linear dependence with n:

$$\sqrt{\sigma_n^2 - (\sigma_n^{\pm})^2} = n\sigma_{coh} \qquad (25)$$

where n is even.

In the present work these procedures were used mainly as cross-checks of the results obtained with the standard method, but they could be considered as an alternate method for noise estimation. Therefore, the fits with equ. (24) or equ.(21) to $\sigma_n^{\pm}$ or with equ. (25) to $\sqrt{\sigma_n^2 - (\sigma_n^{\pm})^2}$ are referred in this paper as Method II.

5.3 Noise in the Tilecal calorimeter

For Tilecal calorimeter, the outside burst pedestal events (selected with trig=4) taken along with physics events were the main source of data for the electronic noise analysis. Whenever possible, alternate sources of information were considered in order to cross-check the results. In this case they were the low energy electron runs, after imposing cuts to eliminate the pions and muons which contaminates the electron beam. The showers produced by low energy electrons are completely contained in the EM calorimeter and the Tile calorimeter part of the physics event (trig=1) represents in fact the electronic noise alone. The selection procedure is illustrated in figure 34 for a 20 GeV electron run. The distribution of the signal from all hadron calorimeter cells as can be seen in the lower left plot of this figure is peaked around zero (more exactly at -0.075 GeV). The conversion factors used:

- 0.034 pC/ADC (amplified channels)

- 136 MeV/pC (this value has been obtained in the section analysing the pion results)

A gaussian fit of this distribution gives 351 MeV for the standard deviation, a value which as is shown later is not very far from the estimated value of the total noise in Tilecal. The difference comes from the fact that after extracting the pedestals, the mean value in each channel is not exactly zero. This deviation also contributes to the width of the total signal. In the noise analysis the data are corrected for this effect.
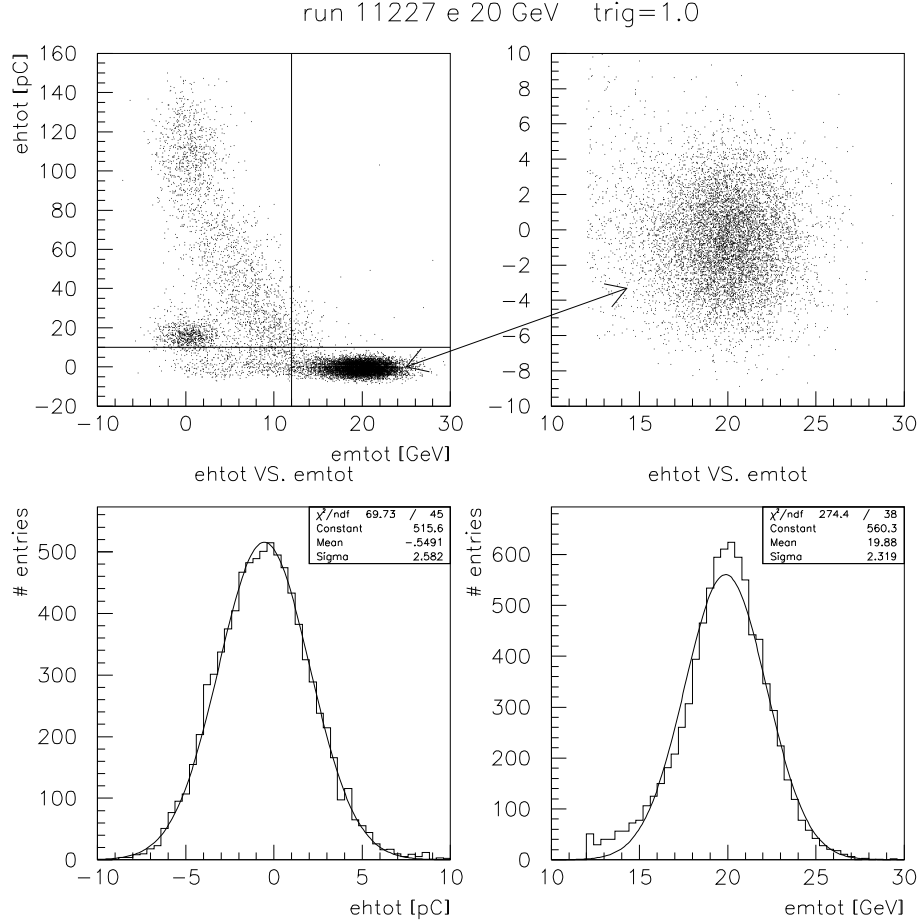
Figure 34: Run 11227 (e 20 GeV, trig=1) events. The cuts are indicated in the upper left plot. The selected sample of electron events (upper right) has a peak around 20 GeV in the total energy in the EM calorimeter (lower right) and around zero in the total energy in hadron calorimeter (lower left)

For those two cases: pedestals (trig=4) and physics events (trig=1), the information in the ntuples is treated differently: ADC counts for pedestals and pC for physics events. When comparisons are made between these two sets of data in those plots the results are transformed in ADC counts. The analysis was done module by module using Method I to fit the values of random and coherent noise. The results are illustrated in figure 35 using pedestals from a pion run and in figure 36 using physics electron events.

The fitted values shown in the plots, converted from ADC counts to MeV are presented in table 17. The r.m.s. values of the noise in each channel vs. channel number indicates which are the most noisy channels, and help to the interpretation of the fit results. There are a few noisy channels: 63, 117, 119, 133 and 139, as shown in the plots of r.m.s. of the noise distribution in the individual channels vs. the channel number in the lower left part of figure 35, or figure 36. The Tile readout channel numbering was made module by module, starting from left to right with the five cells of the first longitudinal sampling of the module and continuing on the other longitudinal samplings, which gives 20 cells or 40 PM's per module. So, the first 40 PM's are for the first module, the PM's from 41 to 80 for the second and so on.

A module by module analysis has shown the influence of bad channels. The presence of more noisy channels is reflected in a larger value of the random noise in that module. Channels close to a noisy one tends to have an increased noise level as can be seen in the lower right plot in figures 35 and 36. This results in an increased coherent noise in a module with a larger number of noisy channel.
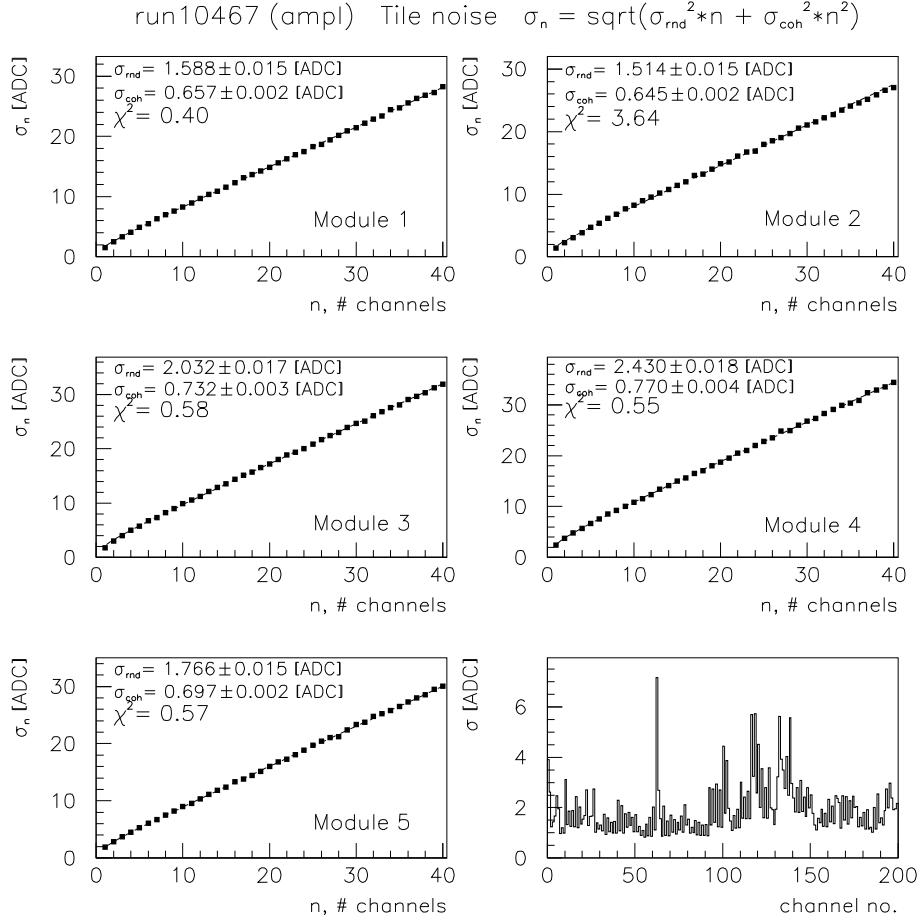
41

Figure 35: Run 10467 (180 GeV π) module by module analysis with Method I, using amplified pedestal (trig=4) events.

The influence of noisy channels is seen to be of short range and the value of coherent noise obtained when the channels from all modules are taken into account (this is closer to the realistic situation met in practice when the energy reconstruction is done) is expected to be smaller than the values obtained in a module per module analysis. The results of the analysis made simultaneously with all modules is shown in figure 37a (determination of σ_{rnd} and σ_{coh} with Method I), figure 37b (determination of σ_{rnd} with Method II), and figure 38 (determination of σ_{coh} with Method II) for the run 10467. A summary of the global analysis made on several runs is presented in Table 18. One can notice a good agreement between the results obtained with the two methods.

The values of the noise components obtained in the global analysis should be taken into account when making estimates of the electronic noise contribution to the energy resolution. The calculated value for the 'electronic term' in the energy resolution parametrization formula for a 5×5 region is 328 MeV, with a contribution of 306.0 MeV from the coherent and of 133.8 from the random noise.

5.4 Noise in the LAr calorimeter

A schematical representation of the electromagnetic calorimeter front face is given in figure 1. Only a partial number of cells was equipped with readout electronics and for these cells three different types of preamplifiers were used: Si, GaAs and 0T. On this figure four different regions are framed in each longitudinal sampling: three of them we denoted by EM and equipped with 0T monogain, Si bi-gain and GaAs bi-gain. A fourth region indicated by UV is characterized
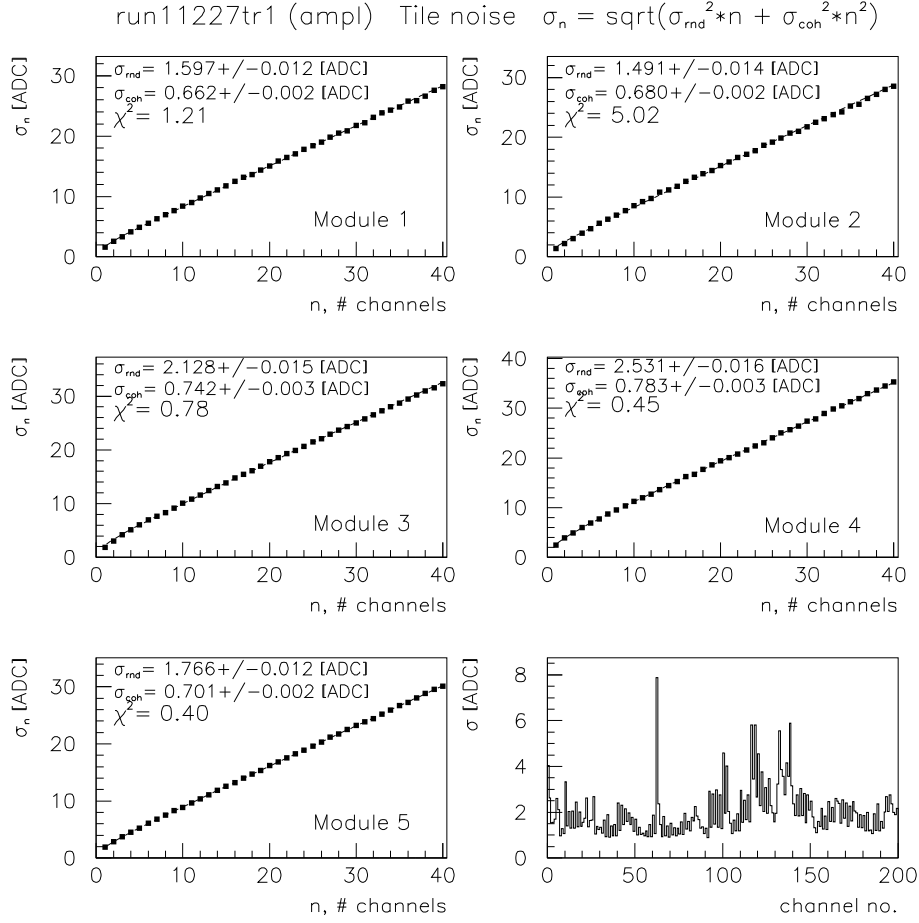
run11227tr1 (ampl)   Tile noise $\sigma_n = \mathrm{sqrt}(\sigma_{rnd}^2 * n + \sigma_{coh}^2 * n^2)$

σ_{rnd}= 1.597+/−0.012 [ADC]
σ_{coh}= 0.662+/−0.002 [ADC]
χ^2= 1.21
Module 1

σ_{rnd}= 1.491+/−0.014 [ADC]
σ_{coh}= 0.680+/−0.002 [ADC]
χ^2= 5.02
Module 2

σ_{rnd}= 2.128+/−0.015 [ADC]
σ_{coh}= 0.742+/−0.003 [ADC]
χ^2= 0.78
Module 3

σ_{rnd}= 2.531+/−0.016 [ADC]
σ_{coh}= 0.783+/−0.003 [ADC]
χ^2= 0.45
Module 4

σ_{rnd}= 1.766+/−0.012 [ADC]
σ_{coh}= 0.701+/−0.002 [ADC]
χ^2= 0.40
Module 5

Figure 36: Run 11227 (e 20 GeV) module by module analysis by Method I using physics (trig=1) events.

by a very fine granularity in U and V in the first sampling and has calorimetric cells of the same size as in the corresponding EM regions in the last two samplings, but equipped with GaAs mono-gain readout. For the pion energy reconstruction, only the information from the EM regions was used and the noise analysis was done only for these channels. In figure 1 the position of the beam impact point is indicated as well. The numbering of the channels is made separately per sampling in each region column by column.

The noise values were extracted from pedestal events and muons (present in electrons or pions physics runs) were used as a cross-check. For muon events, the cells in the direction of the beam and those adjacent to them in all longitudinal samplings have been excluded. There is in general a good agreement between the values obtained from pedestals and from muon events. All the results for run 10795, global and per sampling, are presented in the table 19. There is good agreement between the results obtained with the two methods. The large values of the noise for GaAs in the third longitudinal sampling could be explained by the presence of two very noisy channels out of the 16 channels in this sampling. In figure 39 the fits made per each readout type over all samplings with Method I and Method II are plotted.

5.5   Estimation of the noise contribution to the energy resolution

The noise term coefficient in the energy resolution parametrization formula is evaluated with the global values of the coherent and random noise. It depends on the number of channels (see equ. (21)). Taking into account the results from Table 19 and considering all channels in the EM regions from a 11 × 11 window, centered on the beam impact point (see figure 1), one gets a value of 693.1 MeV for the total random noise and 1174.5 MeV total coherent noise in LAr,

module	pedestals		physics (e^-)	
	σ_{random} [MeV]	$\sigma_{coherent}$ [MeV]	σ_{random} [MeV]	$\sigma_{coherent}$ [MeV]
mod. 1	7.34 ± 0.07	3.04 ± 0.01	7.38 ± 0.06	3.06 ± 0.01
mod. 2	7.00 ± 0.07	2.98 ± 0.01	6.90 ± 0.06	3.14 ± 0.01
mod. 3	9.39 ± 0.08	3.38 ± 0.02	9.84 ± 0.07	3.43 ± 0.02
mod. 4	11.23 ± 0.09	3.56 ± 0.02	11.70 ± 0.07	3.62 ± 0.02
mod. 5	8.17 ± 0.07	3.22 ± 0.01	8.17 ± 0.06	3.24 ± 0.02

Table 17: Tilecal noise results per module, obtained from pedestal events (run 10467, π 180 GeV) and from physics events (run 11227, electrons 20 GeV)
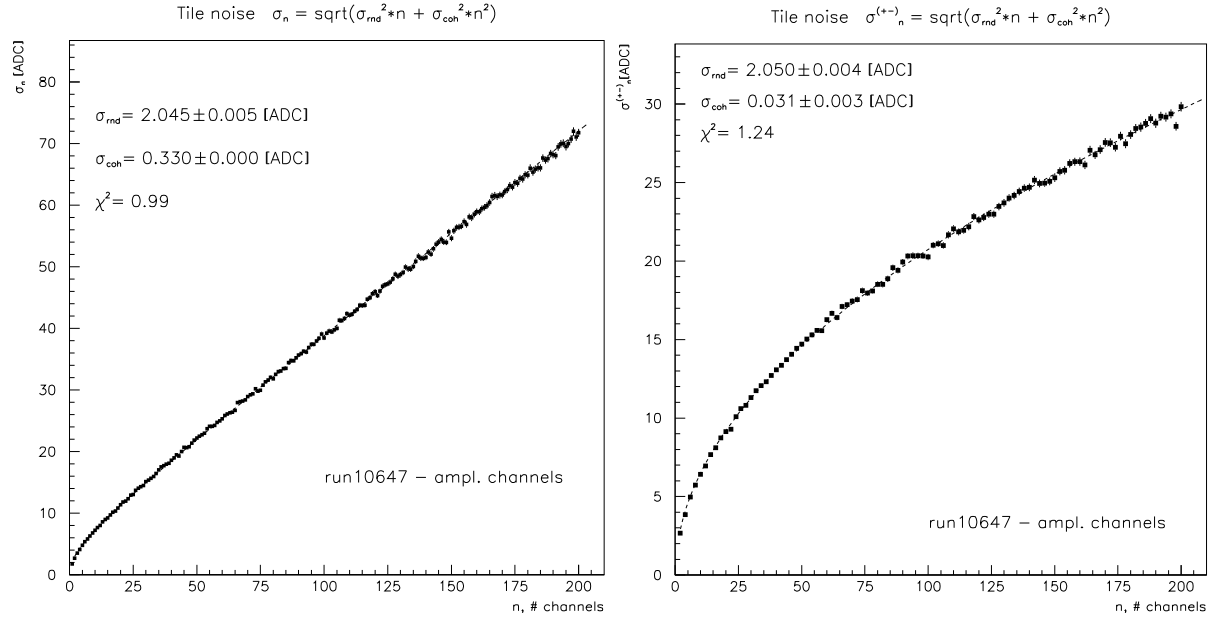

Figure 37: Run 10467 (π 180 GeV) all modules analysis with Method I (on the left) and with Method II (on the right), using amplified pedestal (trig=4) events.

which gives 1363.8 MeV for total noise. With the value of 328 MeV in TileCal and assuming the contributions from Tile and LAr independent, a total contribution of the noise equal to 1404.1 MeV is obtained. This value is slightly lower than the 1.8 GeV term obtained in pion energy reconstruction with the H1 weighting technique. This was not the case in 1994 data where the noise contribution were extimated to be 1.5 GeV, while fitting the energy reconstructed for pions we found a 3.1 GeV noise term.

run no.	no. evn	Method I		Method II	
		σ_{random} [MeV]	$\sigma_{coherent}$ [MeV]	σ_{random} [MeV]	$\sigma_{coherent}$ [MeV]
11227	869	9.06 ± 0.08	1.55 ± 0.01	9.33 ± 0.06	1.51 ± 0.01
11684	669	8.58 ± 0.13	2.10 ± 0.01	9.30 ± 0.07	2.05 ± 0.01
11385	1403	9.29 ± 0.06	1.59± 0.01	9.22 ± 0.05	1.58 ± 0.01
11079	1265	9.20 ± 0.06	1.59 ± 0.01	9.27 ± 0.06	1.58 ± 0.01
10467	6154	9.46 ± 0.02	1.53 ± 0.01	9.48 ± 0.02	1.51 ± 0.01

Table 18: Tile noise results obtained with both methods, for different runs, from a global analysis over all modules.

Samp	type	Method I		Method II	
		σ_{random} [MeV]	$\sigma_{coherent}$ [MeV]	σ_{random} [MeV]	$\sigma_{coherent}$ [MeV]
1	Si	12.51 ± 0.08	2.27 ± 0.02	12.11 ± 0.04	2.33 ± 0.02
2	Si	15.00 ± 0.08	0.66 ± 0.07	14.92 ± 0.04	0.77 ± 0.03
3	Si	17.56 ± 0.13	3.35 ± 0.13	17.73 ± 0.06	3.38 ± 0.02
1+2+3	Si	15.23 ± 0.05	1.32 ± 0.01	14.91 ± 0.03	1.35 ± 0.01
1	GaAs	27.27 ± 0.19	3.34 ± 0.06	28.16 ± 0.11	3.06 ± 0.06
2	GaAs	32.49 ± 0.22	3.12 ± 0.10	31.75 ± 0.14	3.48 ± 0.08
3	GaAs	43.54 ± 0.75	9.51 ± 0.40	44.42 ± 0.33	9.41 ± 0.27
1+2+3	GaAs	32.30 ± 0.14	2.97 ± 0.03	32.32 ± 0.08	2.96 ± 0.03
1	0T	47.74 ± 0.42	11.45 ± 0.08	47.41 ± 0.17	11.55 ± 0.07
2	0T	47.01 ± 0.35	7.77 ± 0.09	47.24 ± 0.17	7.89 ± 0.08
3	0T	47.01 ± 0.42	3.83 ± 0.35	46.36 ± 0.25	4.45 ± 0.26
1+2+3	0T	47.31 ± 0.24	7.63 ± 0.03	47.67 ± 0.11	7.60 ± 0.03
1+2+3	all	31.42 ± 0.08	2.63 ± 0.01	32.03 ± 0.04	2.60 ± 0.01

Table 19: Results obtained with Method I and Method II for the electronic noise in the EM calorimeter cells, for run 10795
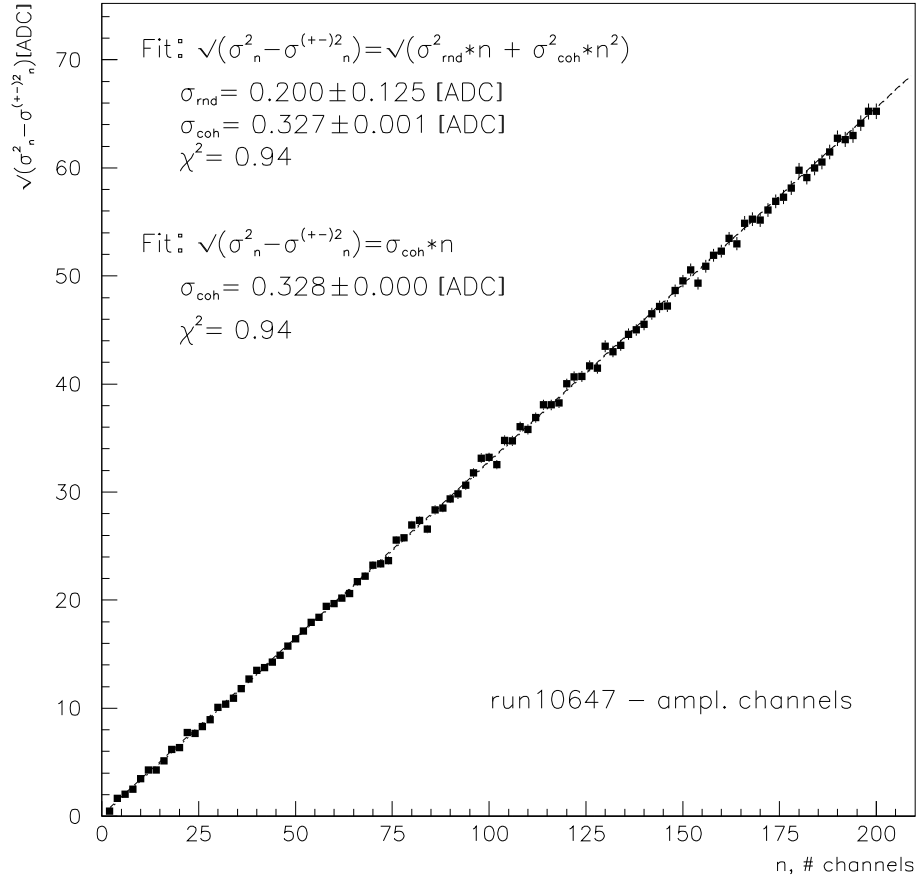
Figure 38: Run 10467 (π 180 GeV) all modules, check of coherent noise linearity , using amplified pedestal (trig=4) events.
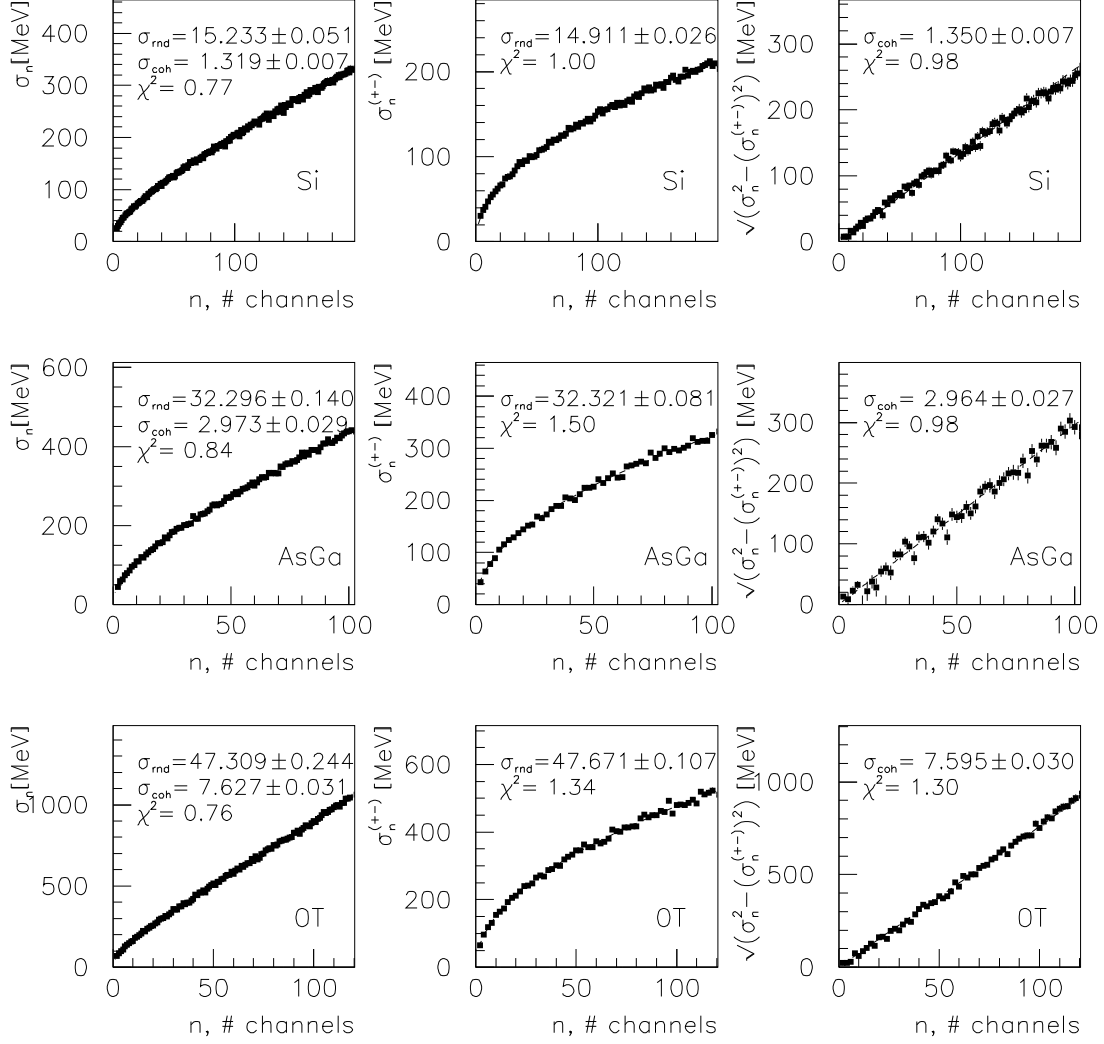
Figure 39: Results of the noise estimation in the LAr, all samplings. In the first column are the results obtained with Method I for σ_{rnd} and σ_{coh}, in the second with Method II for σ_{rnd} and in the third, with Method II for σ_{coh}. The results are for the run 10795 and the units are MeV.

6   Conclusions

The 1996 combined test beam data have been analyzed and compared with the data of the previous test beam performed in 1994.

Electron, muons and pions from 10 to 300 GeV have been reconstructed. The H1 technique to reconstruct pions energy leads to a resolution which can be parametrized as: $[\frac{(41.9\pm1.6)\%}{\sqrt{E}} + (1.8\pm0.1)\%] \oplus \frac{1.8\pm0.1}{E}$

The problem of the high resolution observed for the 20 GeV point in 1994 data, is no more present, and the additional 10 GeV point is in line with the ATLAS calorimetry requirement.

The e/π, longitudinal deposition and punchthrough probabilities are in good agreement with the results obtained in 1994.

A clear muon signal is observed for muons traversing the combined setup.

From pedestal study, the total (LAr+Tile) electronic noise term is expected to be around 1.4 GeV (to be compared with the noise term of 1.8 GeV in the energy resolution parametrization formula).

The people who signed this note are the authors of the final analysis on the combined test beam data. However, many other people contributed directly to this work in the past, so that they cannot be acknowledged individually. Our thanks go to the whole Atlas LAr, Tilecal and DAQ subsystems for all the help given to the authors as well as for the efforts put during the test beam data taking period. A publication will be extracted from this note. Such a publication will also appear as a CALO note, with a properly extended list of authors.

Dan Pantea wish to thank for the hospitality at CPP Marseille, where was done the most part of his contribution to this note.

References

[1] ATLAS Technical Proposal, CERN/LHCC/94-43 LHCC/P2.

[2] The RD3 collaboration: D.M. Gingrich et al, "Performance of a Large Scale Prototype of the ATLAS Accordion Electromagnetic Calorimeter", Nuclear Inst. and Methods A364 (1995) 290-306.

[3] F. Ariztizabal et al., Nucl. Instr. and Meth. **A349** (1994) 384.

[4] Z. Ajaltouni et al. (The ATLAS Collaboration), "Results from a combined test of an electromagnetic liquid argon calorimeter with a hadronic scintillating-tile calorimeter" Nucl. Instr. and Meth. **A387** (1997) 333-351 (PPE preprint PPE/96-178)

[5] O. Gildemeister, F. Nessi-Tedaldi and M. Nessi, Proc. 2nd Int. Conf. on Cal. in HEP, Capri, 1991.

[6] M. Bosman et al. (RD34 Collaboration), CERN/DRDC/93-3 (1993),
F. Ariztizabal et al. (RD34 Collaboration), CERN/DRDC/94-66 (1994)

[7] Lokajicek et al., "Scintillator detector Mu-wall for measurement of charged particles leakage from the TILECAL prototype", ATLAS Internal Note, TILECAL-No-63 (1995)

[8] M. Cobal et al., "Analysis results of the first combined test of the LArgon and TILECAL barrel calorimeter prototypes", ATLAS Internal Note, TILECAL-No-67 (1995)

[9] M.P. Casado, M. Cavalli-Sforza, "H1-inspired analysis of the 1994 combined tes of the Liqui Argon and Tilecal calorimeter', ATLAS Internal Note, TILECAL-No-75 (1996)

[10] A. Ferrari P. Sala, "The Physics of High Energy Reaction", Lecture given at the *Workshop on Nuclear Reaction Data and Nuclear reactor Physics, Design and Safety*, Trieste 1996. Also ATLAS Internal Note, PHYS-No-113.

[11] H. Plothow-Besch, "First Study on the Angular Resolution of Hadronic Showers with the Combined LAr and Tile Calorimeter", ATLAS Internal Note, TILECAL-No-70 (1995)

[12] A. Castera *et al.*, "Analysis of the 1995 liquid argon test beam with a digital readout prototype", ATLAS Internal note, LARG-No-72, 1997, CERN, Geneva, Switzerland.

[13] J.A. Budagov, Y.A. Kulchitsky, V.B. Vinogradov *et al.*, "Electron Response and e/h Ratio of AT-LAS Iron-Scintillator Hadron Prototype Calorimeter with longitudinal Tile Configuration", JINR, E1-95-513, 1995, Dubna, Russia; ATLAS Internal note, TILECAL-No-72, 1995, CERN, Geneva, Switzerland.

[14] E. Moyal, Phil. Mag. **46** (1955) 263.

[15] M. Lokajacek et al., ATLAS Internal Note, TILECAL-NO-xxx (1995).

[16] RD5 Collaboration, Z. Phys. **C60** (1993) 1, RD5 Collaboration, CERN-PPE/95-61

[17] H. Abramowicz et al., Nucl. Instr. and Meth. **A180** (1981) 429.
M. De Vincenzi et al., Nucl. Instr. and Meth. **A243** (1986) 348.

[18] R. K. Bock et al., Nucl. Instr. and Meth. **A186** (1981) 533.

[19] CCFR Collaboration, Nucl. Instr. and Meth. **A245** (1986) 27.

[20] A. Juste, Thesis IFAE,UAB October 1995.

[21] Tilecal collaboration: "Atlas Tile Calorimeter Technical Design Report", CERN/LHCC/96-42, 1996

[22] T. Davídek, R. Leitner: "Parametrization of the Muon Response in the Tile Calorimeter", TILECAL-NO-114, 1997

[23] Z. Ajaltouni et al.: "Response of the ATLAS Tile Calorimeter Prototype to Muons", NIM A 388 (1997), 64-78